

Recent Approaches for Bridging the Pressure Gap in Photoelectron Microspectroscopy

Andrei Kolmakov¹ · Luca Gregoratti² · Maya Kiskinova² · Sebastian Günther³

Published online: 29 January 2016

© The Author(s) 2016. This article is published with open access at Springerlink.com

Abstract Ambient-pressure photoelectron spectroscopy (APPEs) and microscopy are at the frontier of modern chemical analysis at liquid–gas, solid–liquid and solid–gas interfaces, bridging science and engineering of functional materials. Complementing the current state-of-the-art of the instruments using differentially pumped analyzers, we survey in this short review several alternative APPEs approaches, developed recently in the scanning photoelectron microscope (SPEM) at the Elettra laboratory. The reported set-ups allow for performing dynamic near-ambient pressure experiments without introducing additional differential pumping stages. They include implementation of pulsed-gas injection in the vicinity of samples or placing the sample inside reaction cells with very small apertures. The major part of the review is dedicated to construction and performance of novel environmental cells, where ultrathin electron-transparent but molecularly impermeable membranes are used to isolate the gas or liquid ambient from the electron detector operated in ultra-high vacuum (UHV). We demonstrate that two-dimensional materials, such as graphene and derivatives, are mechanically robust to withstand atmospheric–UHV pressure differences and are sufficiently transparent for the photoelectrons emitted

from samples immersed in liquid or gaseous media. Representative results illustrate the performance of reported APPEs approaches using tunable synchrotron X-rays, combined with the sub-micrometer lateral resolution of SPEM. They demonstrate the unique opportunities for addressing the chemical composition and electronic structure of surfaces and interfaces under realistic operation conditions with unprecedented lateral and spectral resolution.

Keywords Ambient pressure XPS · Graphene membranes · Environmental cell · Microscopy

1 Introduction

Fundamental understanding and control of processes occurring at surfaces and interfaces can guide the design and optimization of catalysts and materials used in chemical industry, energy and electronic devices and also will respond to many open questions in biomedical research. Therefore, there is an increasing demand for detailed in situ surface analyses of functional matter under realistic working conditions. Only in the last decade the most powerful surface sensitive method, photoelectron spectroscopy (PES), also known as X-ray photoelectron spectroscopy (XPS) or electron spectroscopy for chemical analysis (ESCA) [1], has really overcome the pressure gap. Today ambient pressure PES (APPEs) allows for in situ PES experiments that were a dream half a century ago. The first APPEs attempts in liquid ambient were made by Kai Siegbahn's group in the early 1970s, followed by the exploration of a variety of experimental approaches, such as liquid beams jets [2–4] or flying droplets [5]), and wetted specimens [6]. These efforts culminated recently by

✉ Andrei Kolmakov
andrei.kolmakov@nist.gov

✉ Sebastian Günther
sebastian.guenther@tum.de

¹ Center for Nanoscale Science and Technology, NIST, Gaithersburg, MD 20899, USA

² Elettra - Sincrotrone Trieste SCpA, Area Science Park, 34149 Trieste, Italy

³ Chemie Department, Technische Universität München, Lichtenbergstr, 85748 Garching, Germany

implementation of differentially pumped electron analyzers, using both laboratory X-ray sources [7–11] and synchrotron radiation facilities [12–15]. The progress of APPEs with multiple applications in studies of solid/gas and solid/liquid interfaces is comprehensively reviewed in Refs. [16, 17] and the fast growing number of researchers using these instruments are clear demonstration of the impact and maturity of this methodology. Using synchrotron light for APPEs has several advantages, namely signal gain due to the higher photon flux confined in relatively small spot size of maximum a few hundreds micrometer, and tunability of the X-ray energy that enables optimizing the ionization cross section for the electronic levels under consideration and varying the escape depth of emitted electrons.

The tunability of synchrotron light also allows another spectroscopy that complements PES, namely X-ray absorption spectroscopy (XAS). This technique can use alternative detection modes, based on monitoring the signal of transmitted photons, the total emitted electron/Auger or fluorescence yield as a function of the incident beam photon energy [18]. The XAS spectrum has two distinct parts: the X-ray absorption near-edge structure (XANES), covering the energy range up to 50 eV above the atomic absorption edge, and the extended X-ray absorption fine structure (EXAFS) region above this photon energy. The XANES provides chemical characteristics based on the X-ray induced resonant electronic transitions from the core levels into unfilled electronic states, governed by the well-established selection rules, and serves as a site-specific probe of local charge state, coordination, and magnetic moment of absorbing atoms. Compared to XPS with soft X-rays, which is extremely surface-sensitive [19], complementary XANES spectroscopy measuring total electron yield increases the probing depth to 10 nm, so that one can probe the subsurface region and buried interfaces as well [20, 21]. Using synchrotron light with circular (left–right) or linear (vertical–horizontal) polarization adds information on average magnetic moment and symmetry of the chemical bonds [21].

However, the currently operational APPEs instruments, both in laboratories and synchrotron facilities, are limited in lateral resolution and cannot satisfy the increasing needs of exploring surface and interface properties at submicron and nanoscopic scales, where inhomogeneity in composition and/or morphology is very common in all technologically important materials. More than two decades ago, the demand to characterize the materials at their natural length scales has pushed the development of two major types of X-ray photoelectron microscopies operated with synchrotron light [22–25] and it is appealing to adapt such instruments also for working at ‘ambient’ pressures. However, such adaptation is practically impossible for the

X-ray imaging photo emission electron microscope (XPEEM) [23, 24] that uses electron projection optics to produce a magnified image on the detector plane. These microscopes can reach a lateral resolution better than 10 nm, but the high fields at the sample (of the order of 10^6 – 10^7 V/m), needed for collection efficiency and lateral resolution, exclude working at ambient pressures. The other photoelectron microscopy type, the scanning photoelectron microscope (SPEM) [22, 23, 25] can be described as a classical PES instrument with photon-focusing optics forming an X-ray microprobe. It can reach a lateral resolution of 50 nm when using zone plates (ZPs) as focusing elements. However, the ZP optical set-up, namely the short distance between the focusing system and the sample together with the grazing accepting geometry of the electron analyzer, imposes severe geometrical constraints at soft X-rays energies that need to be solved.

In this paper, after an overview of several routes to further the APPEs methodology, we discuss the set-ups recently developed and tested at the Elettra laboratory that also overcome the aforementioned constraints for SPEM operation at ambient pressure. The membrane-based approaches suitable for all type of instruments with electron detection are extensively discussed, including information on the recent progress in membrane characterization and fabrication technology.

2 APPEs Concepts

2.1 Differentially Pumped APPEs

A key feature of the APPEs technique is performing experiments with samples exposed to their working environment, e.g. a gaseous atmosphere at elevated pressure or a liquid environment. The major problem to be solved in construction of APPEs instruments is the short inelastic mean free path (IMFP) of photoelectrons (PEs) travelling in dense phases [19]. Three possible strategies, sketched in Fig. 1, can be used to minimize the photoelectron elastic and inelastic scattering and thus to meet the requirements of APPEs experiments.

In the first set-up, the differentially pumped analyzer is attached to the chamber hosting a conventional sample holder (Fig. 1a). As sketched in the figure, an aperture of radius R , placed at the entrance of the electron analyzer-lens system at a distance d from the sample, acts as a pressure reducing orifice between the sample environment (p_{HP}) and the first pumping stage of the spectrometer (p_{SP}). Obviously, decreasing R will increase the pressure difference between the sample environment and the electron analyzer, but at a given sample distance d , this also cuts the acceptance angle of the spectrometer, reducing the

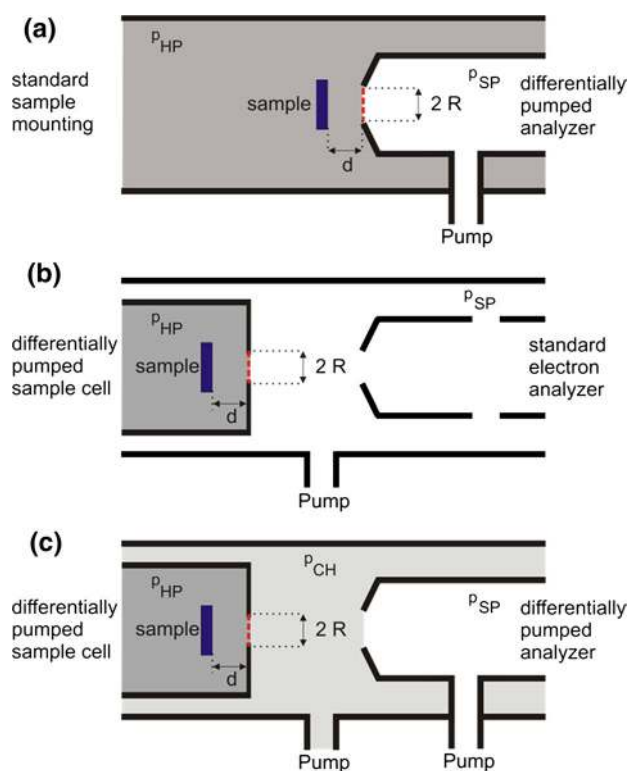


Fig. 1 Possible arrangements of electron spectrometer and sample environment for APPES. **a** Chamber with conventional sample mounting at a distance d in front of a differentially pumped electron analyzer with an aperture of radius R placed at the analyzer entrance. **b** Conventional electron analyzer combined with a differentially pumped sample cell and **c** Combination of a differentially pumped sample cell with a differentially pumped electron analyzer. The *red-dashed lines* indicate the positions, where exchangeable electron-transparent membranes may be used in order to isolate the nearby compartment

detection efficiency. Thus, a compromise between detection efficiency and the inelastic mean free path of electrons in the dense medium has to be found, which determines the achievable pressure in the sample area. The distance, d , between the sample and the aperture should not be smaller than $d \approx 2R$, as it ensures a local pressure at the sample surface comparable ($\approx 95\%$) to the overall pressure p_{HP} . It should be noted that the use of focused photon beams allows for smaller apertures without a significant signal loss. Depending on the X-ray beam spot size, the analyzer dimensions and the number of differential pumping stages, the achievable pressure at the sample in laboratory instruments can be 1 hPa [10] reaching even 30 hPa in the recent report [11]. Synchrotron-based APPES systems operate at pressures of the order of 10 hPa [12, 16] reaching pressures higher than 100 hPa in a recent apparatus using an aperture size of 50 μm [26].

The second approach, sketched in Fig. 1b, combines a standard (non-differentially pumped) electron analyzer with a reaction cell, which has its own gas inlet and

differential pumping system. Here, the aperture of the cell in front of the sample provides the required pressure reduction between p_{HP} and p_{SP} with the same trade-offs as the ones of the first concept, described above. It should be noted that the use of focused photon beams is beneficial for both concepts, because it allows for higher pressures via placing smaller apertures. As reported in Sect. 3.1, the submicrometer photon beam at the ESCA microscopy beamline at Elettra enables measurements at pressures up to 1 hPa inside such reaction cells.

As illustrated in Fig. 1c, the two set-ups can also be combined, resulting in a compartment at an intermediate pressure p_{CH} ($p_{HP} > p_{CH} > p_{SP}$). This combination is advantageous, since the walls of the surrounding vacuum chamber are not exposed to high pressure, which allows for quick switching between high pressure and UHV conditions [14, 17]. In order to obtain a sufficiently intense photoelectron signal, the differentially pumped sample cell is placed close to the electron analyzer entrance. As will be discussed in the following section, membrane-based reaction cell concepts allow for moving the sample cell away from the analyzer entrance, which can be beneficial in many applications.

2.2 Membrane-Based APPES

Another concept complementing differential pumping in APPES is based on use of electron-transparent but molecular-impermeable membranes to separate the sample compartment from the UHV of the electron analyzer. Development of such a PES-through-membrane approach is inspired by the successful photoelectron spectroscopy and microscopy of buried interfaces for a wide range of excitation energies spanning ultraviolet (UV) [27], soft X-rays [28] to hard X-rays [29, 30]. The membrane can be considered as an overlayer with a thickness comparable to the IMFP, so that the signal from the immersed sample is directly related to the classical signal attenuation by overlayer films in surface science [31]. Thus, the attenuation due to inelastic electron scattering by a membrane of thickness d can be evaluated using known databases [31–33] and software [34], discussed in more details in Sect. 3.3. For example, the IMFP of photoelectrons with energies of a few 100 eV is of the order of 1 nm inside the membrane material. Assuming that 90% loss of PES signal from the encapsulated object is acceptable, a 1 nm thick membrane sealing an environment at atmospheric pressure requires the sample surface to be placed at a distance of 1 μm below the membrane, which is sufficient to maintain a thermodynamic equilibrium with the ambient. It is important to note that the minimal membrane thickness and the sample-to-membrane distance limit can be further relaxed if hard X-rays are used, since the high

kinetic energies photoelectrons have longer IMFPs [35, 36].

The use of electron-transparent membranes can be advantageous to the aforementioned differential pumping approaches: sealing with a membrane is indicated by a red dashed line for the three set-ups illustrated in Fig. 1. In all three cases, even if the membranes are imperfect and not 100 % impermeable, the limitation on the maximum achievable sample environment pressures can be greatly relaxed, as described in the following:

- (1) The sample area from which photoelectrons are collected is not limited anymore by the size of pressure-limiting apertures and can therefore be significantly increased. In addition, much larger pressure differentials can be allowed for all APPES concepts sketched in Fig. 1. For example, as long as a molecular-flow regime is sustained, it should still be possible to increase the pressure differential by two orders of magnitude even if 1 % of the membrane area is holey [37].
- (2) The restriction $d \approx 2R$ is not anymore valid when using a membrane, since the electron path inside the dense medium depends only on the sample-membrane distance. This relaxed constraint will allow for denser phases in the sample area, while keeping the same spectral quality simply by reducing the distance to the analyzer.
- (3) Using arrays of micro-membranes rather than a single membrane (see Sect. 5), macroscopic sample areas can be explored using the setup sketched in Fig. 1b. Hence, high-quality APPES studies can be done using standard laboratory-based equipment.
- (4) Combining a membrane-sealed sample cell with a differentially pumped analyzer can boost the performance of existing APPES instrumentation as outlined in the points (1)–(3). The additional advantage of this combination (see Fig. 1c) is that the sample cell can be easily repaired after a membrane failure. In addition, the membrane-sealed cell may be placed further away from the analyzer entrance, thereby protecting the delicate electron lens system in case of membrane failure. This advantage is especially important when dealing with samples in a liquid environment, where membrane failures may lead to ejection of a liquid jet (see Fig. 2).

It should be noted that all considerations above apply to APPES of liquids or samples in liquid environment, assuming that any liquid leakage and its related partial pressure does not exceed the capability of the pumping system. Since this problem has to be avoided, gas tight membranes of maximum mechanical, chemical and radiation stability are essential for such studies and are still the

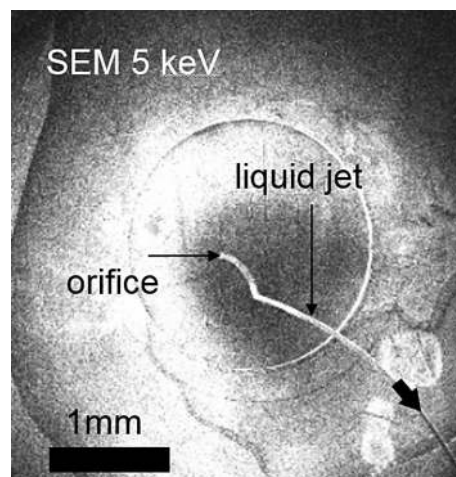


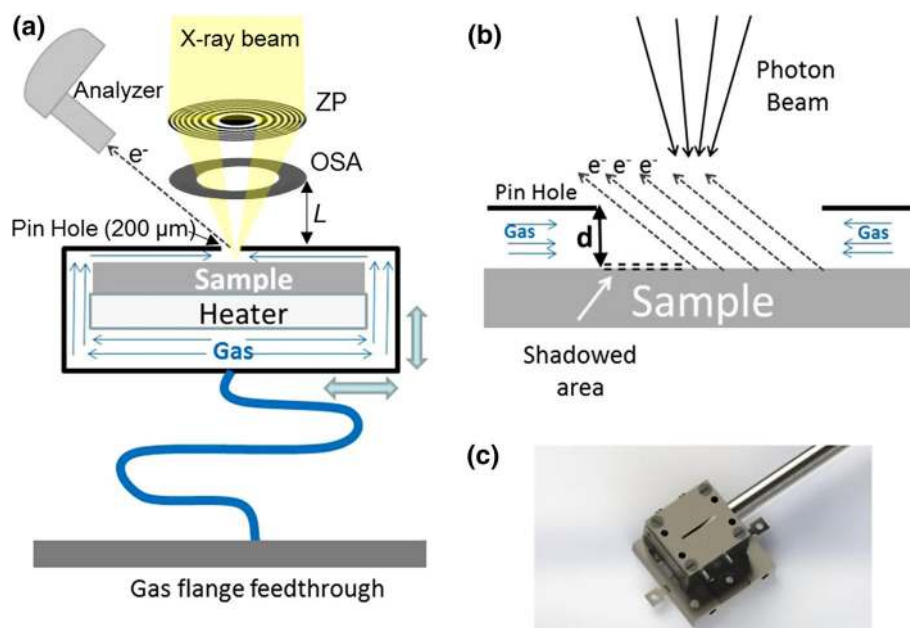
Fig. 2 SEM movie snapshot of a liquid jet ejecting into the vacuum chamber from a sealed liquid cell upon disruption of a graphene membrane. The ejection continues until the Laplace pressure at the orifice equilibrates with the pressure differential between the vacuum and interior of the cell

objective of our research. The recent progress in development and characterization of highly electron transparent membranes is discussed in Sects. 3.3 and 4 of this paper.

3 APPES Microscopy

As noted in the introduction, scanning photoelectron microscopes can be adapted to ambient-pressure experiments overcoming the constraints imposed by the presence of focusing system, sample scanning stages, and grazing incidence geometry of the electron analyzer (see the sketch in Fig. 3a). The best beam demagnification is achieved by using ZP diffractive optics and a pinhole serving as an order sorting aperture (OSA) for blocking the undesired high order diffraction [38]. As illustrated in Fig. 2(a) the focusing system is placed along the X-ray beam, which is normal to the sample surface. In APPES, one should carefully evaluate the constraints imposed by the distance L between the sample and the OSA (Fig. 3a). This distance depends on several parameters and increases with increasing X-ray energy, ZP diameter and ZP outermost zone width. The usual ZP to sample distance is of the order of 3 mm to 10 mm using soft X-rays, since the outermost zone width that determines the microprobe size (lateral resolution) should be in the few tens nm range and microfabrication and use of ZPs with diameter beyond 300 μm is challenging. Considering that the presence of an OSA further restricts the access to the sample, the realization of the classical differentially pumped analyzer APPES geometry where the sample to analyzer distance can be even less than 1 mm, is practically impossible.

Fig. 3 **a** Sketch of the SPEM set-up with the reaction cell and its main components. **b** Large-scale sketch outlining the probed sample area. In order to illustrate the shadowing effect, the distance d is expanded. **c** Photo of the cell mounted on the sample holder which can be inserted in the scanning unit of the SPEM



Placing the X-ray focusing set-up at a grazing incidence angle with respect to the sample surface normal, as used in classical PES, introduces severe distortions in the microprobe dimensions and does not relax sufficiently the sample-analyzer distance issue. However, ambient pressure SPEM (AP-SPEM) can be performed using electron transparent membranes to separate the sample environment from the electron and/or X-ray optics, as we have already demonstrated [39, 40] and as is discussed in Sect. 3.3. Additionally, we have developed two other simpler set-ups, a reaction cell using only a small orifice for probing the sample (Sect. 3.1) and a dynamic high-pressure gas injection system (Sect. 3.2) that can partially overcome the limitations imposed in ZP-based SPEMs when working at near-ambient pressures. These different set-ups were designed and constructed to fit to the SPEM instrument, operated at the ESCA microscopy beamline of the Elettra synchrotron research center [41], but also are applicable to other photon-in/electron-out or electron-in/electron-out instruments of this type.

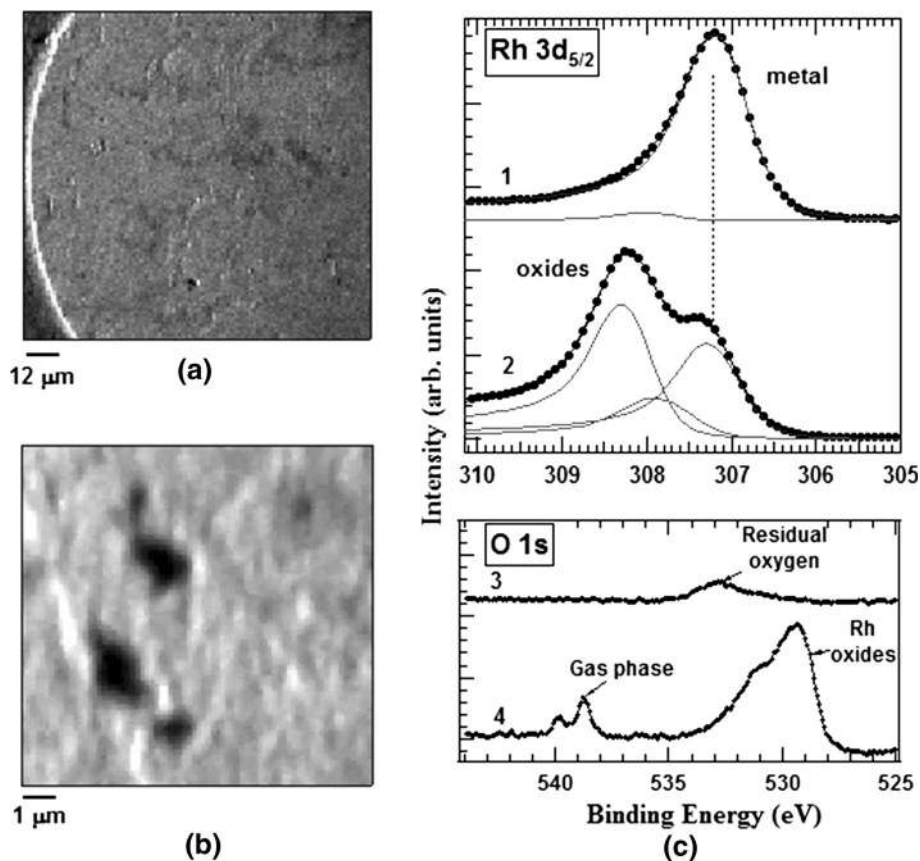
3.1 Reaction Cells for SPEM

The general concepts for construction of reaction cells are not new: retractable cells bridging near ambient pressure up to 30 hPa and UHV have already been offered by companies providing laboratory XPS instruments [11]. The specific approach used in the cell design for SPEM further exploits the advantage of using a focused X-ray beam. The SPEM reaction cell, illustrated in Fig. 3a), is vacuum sealed and has a small pinhole of 200 μm diameter on the front plate. The X-ray microprobe (50–100 nm diameters)

illuminates the sample placed at a distance of 30–40 μm behind the pinhole (see Fig. 3b). For such small distances the shadowing effect is insignificant and photoelectrons from a sufficiently large sample area can be collected by the electron analyzer mounted at 60° with respect to the X-ray beam. The reactive gases were controllably delivered into the cell via flexible tubing, connected to a flange with a needle valve. The pumping speed of the vacuum chamber permits achieving pressures up to 1 hPa inside the cell, while keeping the background pressure of the SPEM chamber below 10^{-5} hPa (upper safe limit for performing photoelectron spectroscopy). An encapsulated heater, attached on the rear side of the sample, is used to vary the sample temperature in the range 300 K to 773 K. The cell assembly was mounted on a sample holder (Fig. 3c), attached to the x–y scanner, which was used in the SPEM imaging mode and also for fine positioning at selected locations in the micro-spectroscopy mode. All parts of the cell, including the heater and the thermocouple feed throughs, were made of UHV compatible materials to avoid parasitic degassing inside the enclosure upon heating.

The cell performance was tested using the well-known oxidation and reduction of a metal Rh surface by measuring the evolution of Rh 3d and O 1 s core levels acquired from an unpolished Rh foil, mounted inside the high pressure cell and exposed to oxygen and hydrogen. Figure 4a and b show large- and small-scale Rh images, acquired using the photoelectron analyzer tuned to the Rh 3d_{5/2} core level energy window. The images represent the lateral variations of the photoemission signal integrated over the whole energy window, including also the

Fig. 4 $100 \times 100 \mu\text{m}^2$ (a) $12 \times 12 \mu\text{m}^2$ (b) Rh $3d_{5/2}$ images of Rh foil inside the cell; c Rh $3d_{5/2}$ and O 1s spectra taken at representative microspot of the Rh foil before (1), (3) and after (2), (4) oxidation. The measurements were made with a photon energy of 650 eV



background. Under these settings the observed darker and brighter features are topographic contrast, i.e. local enhancement or attenuation of the emitted photoelectrons, generated by the structural imperfection of the Rh surface [42]. These well-resolved structures prove that the typical submicron resolution of the SPEM instrument is preserved, i.e., the cell setup does not deteriorate the spatial resolution of the microscope.

The lineshape of the top Rh $3d_{5/2}$ spectrum 1 in Fig. 4c) is typical for a sample that was oxidized and contaminated during unavoidable short exposure to air before being introduced into the cell, where it was annealed at 573 K in the ambient of 1 hPa of $\text{H}_2(\text{g})$ for 60 min in order to remove the formed oxide layer and other contaminants. The spectrum, deconvoluted by using Doniach-Sunjich functions (black solid lines), reveals a dominant metallic Rh component at a binding energy (BE) of 307.2 eV and a tiny peak at 307.8 eV, indicative of the presence of residual sub-stoichiometric surface oxides [43]. This result is clear evidence that the annealing at 1 hPa H_2 exposure had rather effectively removed the oxide and usual C contaminants, which is not possible for H_2 exposures at the maximum pressure of 5×10^{-5} hPa allowed in the SPEM chamber. The same surface was then exposed to 1 hPa O_2 for 30 min, keeping the temperature of the sample at

573 K. The measured Rh $3d_{5/2}$ spectrum after our oxygen treatment (spectrum 2 in the Rh $3d_{5/2}$ panel of Fig. 4c) is dominated by a new peak located at 308.3 eV BE, corresponding to Rh_2O_3 [44]. The observed changes in the Rh 3d and O 1s spectra after oxidation are in fair agreement with prior results for Rh films and Rh polycrystalline foils, oxidized at ambient pressures where the observed two components were attributed to of Rh_2O_3 and $\text{RhO}_2/\text{RhOOH}$ species [45, 46].

Clear demonstration that the sample inside the cell was exposed to an O_2 pressure of the order of hPa, required for advanced Rh oxidation, are the O 1s core level spectra. The O 1s spectrum 3 in Fig. 4c, measured after the initial treatment in H_2 , appears as a tiny broad feature peaked at ~ 533 eV, matching a residual suboxide [44]. This is also confirmed by the small high BE component in the corresponding Rh $3d_{5/2}$ spectrum 1. As in the case of the Rh $3d_{5/2}$ spectrum, the line shape and position of the O 1s spectrum drastically changes when the Rh sample is exposed to 1 hPa O_2 , evidenced by spectrum 4, where two new distinct doublet spectral features appear. The more intense doublet is dominated by a component located at ~ 529.5 eV and weaker one at ~ 531.5 eV. The second nicely resolved doublet within the 538.5 to 540 eV range corresponds to gas-phase oxygen molecules inside the cell,

ionized by the impinging X-rays. The line shape and intensity of the O 1 s spectral feature from the gas phase oxygen confirms that the cell allows hPa pressure levels to be reached. This result demonstrates that indeed using the cell the Rh has reached an oxidation state that is not possible under high vacuum conditions [25].

3.2 Dynamic Pressure System

The dynamic ‘high’ pressure approach (DHP) is based on the control of an amount of pulsed gas, injected in the vicinity of the sample, without exceeding the global pressure limits required for the SPEM operation [47]. The local pressure around the sample is controlled by fine tuning of the spatial and time profile of a collimated gas jet, directed towards the sample. In the DHP set-up, sketched in Fig. 5a), the pulsed jet of gas is formed by a thin needle, avoiding any interference with the X-ray optic system and electron analyzer.

As described in Ref. [47], the series of gas jet shots at a fixed repetition rate and duration are obtained by using a computer-controlled pulsed valve. Each pulse generates a short burst of gas pressure at the sample (up to few hundreds hPa) confined in a small volume. If the duration and the repetition rate of the shots are properly tuned, the global background pressure does not exceed the limits imposed by the pumping speed of the vacuum system. In order to achieve the desired control of the gas pulses, a valve with sub-millisecond temporal response is needed. The valve/needle configuration is designed to eliminate any possible dead volume, in order to reduce the time for recovering the background pressure after each pulse.

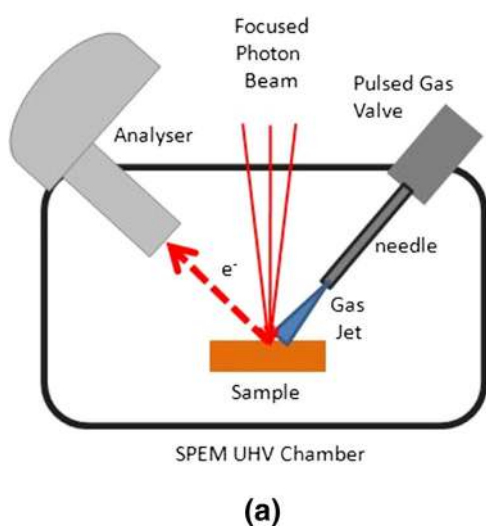


Figure 5b) shows the measured time profiles of the pressure values at the sample and inside the electron analyzer, using 350 kPa O₂ gas pressure behind the pulsed valve. For these measurements, instead of a specimen, a pressure micro-detector was placed on the sample stage. One can see that for 200 hPa oxygen pulses with repetition rate of 0.35 Hz the global pressure in the vacuum chamber remains in the 10⁻⁵ hPa range. The data show that under these conditions, the global pressure recovers very fast to its standard UHV level.

The performance of the DHP system was tested by monitoring the oxidation of Ru, another extensively studied metal. A polycrystalline unpolished Ru sample with an average crystal grain diameter of 1–10 μm was first cleaned by high-temperature annealing using alternating cycles of H₂ and O₂ ambient. Figure 6a and b show the Ru images taken after cleaning by acquiring the photoelectrons emitted in the energy window of the Ru 3d_{5/2} core level. The Ru 3d_{5/2} spectrum of the resultant clean surface, labeled as ‘‘UHV’’ in Fig. 6e, confirms that the metallic Ru component is the dominant feature. As in the case of the Rh foil (see Fig. 4), the contrast of the Ru image (a) is exclusively generated by the surface topography and outlines the grainy structure of the Ru surface, which obscures the true chemical contrast. By processing the clean surface Ru image to remove the topographic artefacts [42], we obtained image (b) showing uniform contaminant-free Ru surface.

The Ru sample kept at 790 K was oxidized in situ using the O₂ pulses provided by the DHP system. The Ru 3d_{5/2} image after oxidation (c) appears similar to the one before oxidation, since again the topography dominates the

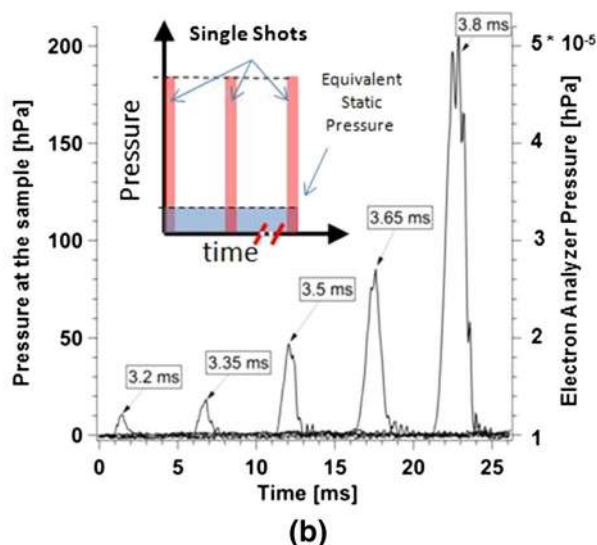


Fig. 5 **a** Sketch of the DHP set-up adapted to the SPEM apparatus [47]. **b** Time profiles of the pressure values at the sample (left axis) and inside the electron analyzer (right axis) for different pulse

durations of a pulsed valve fed by an O₂ gas pressure of 350 kPa. The inset illustrates the working principle of the DHP approach

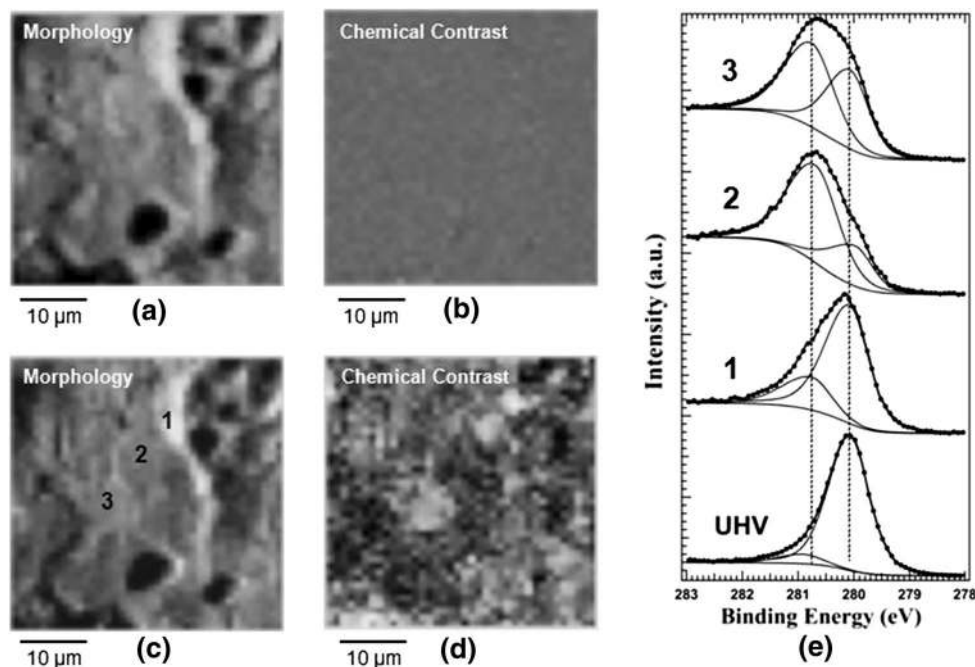


Fig. 6 **a** and **c** Raw Ru $3d_{5/2}$ images of a clean and oxidized surface, respectively, where the topography obscures the chemical contrast. **b** and **d** Ru chemical maps, obtained after removal of the dominant topography contribution in **a** and **c**. In **d** the brighter features correspond to lower oxidation state; **e** Ru $3d_{5/2}$ spectra taken before (UHV) and after oxidation in different positions 1, 2, 3, as indicated in

image **c**. The deconvolution of the spectra clearly shows the different weight of the oxide component at 280.8 eV. Oxidation conditions: pulse duration 3.2 ms, repetition rate of 0.35 Hz and O_2 pressure behind the valve of 350 kPa. The data acquired from the oxidized surface were taken after 600 pulse shots

contrast. However, after processing the images for removal of the topography one can clearly see that the initial clean Ru surface (Fig. 6b) is chemically uniform, also confirmed by the Ru 3d spectra taken at different points. On contrary, after oxidation the processed image in Fig. 6d shows variations in the contrast level, indicating inhomogeneity of the oxidation. In fact, after removing the dominant topographic contrast from (c) we obtained the chemical map, where the darker areas correspond to a lower oxidation state, i.e. the Ru oxide component is less pronounced. This inhomogeneity of the Ru oxidation state is confirmed by the Ru $3d_{5/2}$ spectra measured in different positions, labeled as (1), (2), (3) in Fig. 6c. The difference in the line shapes of these three Ru spectra in Fig. 6e reflects the different weight of the oxide component, due to well-known structural dependence of the oxidation rate [48]. The most intense oxide component is present in region (2) while it is the least intense in the region (1). Comparing (c) and (d) one can indeed find some correlation between the individual surface grains and the attained oxidation state.

The good performance of the DHP system was also verified by oxidizing a Si (111) surface and comparing the oxidation time evolution with that obtained by exposing the surface to a static pressure [47]. The results have

demonstrated that the oxidation of the Si (111) sample at the DHP conditions is equivalent to a static case, where the pressure is kept between 10^{-3} and 10^{-2} hPa, about 3 orders of magnitude higher than the maximum gas pressure allowed for the photoemission system in operando. The DHP system has already been successfully used for: (1) an in situ monitoring of the chemical evolution of the electrodes in a Ni/Y-stabilized zirconia (YSZ)/Mn solid oxide fuel cell occurring in a $H_2 + O_2$ or $CH_4 + O_2$ ambient [49, 50] and (2) an in situ study of the polymer-exchange membrane fuel cell under polarization [51].

3.3 Membrane-Based Approaches for the SPEM

Enclosed cells with Si_3N_4 or SiO_2 membranes have routinely been used for in situ X-ray absorption and transmission spectroscopy [52–57]. Since the membrane thickness capable of withstanding 100 kPa atmospheric pressure differential exceeds 10 nm, they can be penetrated only by photoelectrons with high kinetic energies (in excess of few keV), as has been demonstrated recently for APPES with hard X-rays [35, 58–60]. The limitations, imposed by the thickness of Si_3N_4 and SiO_2 membranes have been overcome by novel two-dimensional (2D) materials, such as graphene (G), graphene oxide (GO),

hexagonal boron nitride (h-BN) etc. [39, 40]. These 2D materials have been found to be ideal for APPEs with soft X-rays, since they combine electron transparency even for photoelectrons with kinetic energy of few 10 eV with molecular impermeability and a record high mechanical strength [39, 40]. In the following sections, we review our recent activities in fabrication and characterization of electron transparent membranes tested with the SPEM operated at the ESCA microscopy beamline of the Elettra synchrotron light source [41].

3.3.1 Fabrication of High Quality Suspended Graphene-Based Membranes

Graphene oxide (GO) was the first 2D material tested as an electron transparent window for APSPEM and SEM environmental cells (E-cells). GO membranes are attractive due to well-developed high yield chemical exfoliation protocols coupled with their large scale liquid processability of GO colloids (see recent review [61] and references therein). Due to their amphiphilic properties, GO flakes segregate at air–water or water–solid interfaces and easily form controllable membranes when using Langmuir–Blodgett (LB) or simple drop casting methods [39, 62–66]. As prepared, the GO membranes made of interlocked GO flakes have selective permeation properties promoting the intercalation and diffusion of water between stacked GO flakes that make them excellent filtering media [63, 67, 68]. To make these GO membranes suitable for APPEs, one can adopt the following strategies: (1) prepare GO electron transparent windows which are made of an individual single (or multilayer) GO flake; (2) use a GO membrane window which has less than one percolating channel for water. Since the amount N of percolating channels over an orifice of diameter D scales as $N \sim (D/L)^2$ (here L is the average size of the GO flake) [63], one can make a molecularly impermeable membrane when $D < L$. In spite of the fact that GO flakes can be as large as hundreds of microns, the practical size of the orifice is below 10 microns due to the limited mechanical stability of the membrane under 100 kPa differential pressure.

We performed comparative tests with GO and graphene (G) membranes [39, 40] (see Sect. 3.3.2) and found that GO is less appealing as a membrane material for liquid APPEs for the following reasons. First, as already mentioned above, GO can be water permeable if the size of the electron transparent window exceeds the average size of an individual GO platelet. Second, the thickness of the dip coated or drop casted GO membranes cannot be reliably controlled. Third, GO is non-conductive so that PES measurements require an energy reference. Finally, we found that GO is prone to photo-reduction under focused

X-ray beams. Hence, graphene based membranes, being mechanically extremely robust, chemically stable [69, 70], easier to handle [71] and electrically conductive [72], are a much better choice. The superior performance of graphene membranes makes them appealing, but the fabrication of high-purity suspended G membranes with high yield needs further development. In the following, we discuss the recent progress and the problems to be solved for improving the quality of fabricated G membranes.

Membranes made of mechanically exfoliated single crystal graphene are inherently clean, have superior mechanical stiffness (1 TPa) [69] and, therefore, are nearly ideal for fabricating electron transparent windows of a few micron diameter. However, the necessity for a high yield dictates the use of chemical vapor deposition (CVD) grown graphene for membrane fabrication. CVD graphene, grown using standard protocols is a polycrystalline material with single crystalline domains of diameters ranging from sub μm to a few μm [73–75]. It has been reported that the presence of domain boundaries in the suspended G film [73], worsen the mechanical strength of suspended graphene by more than an order of magnitude. There is then an increased propensity for graphene tearing along the domain boundaries. Figure 7a shows this tendency for membrane rupture along the domain boundaries present in a medium quality graphene after it was transferred onto an orifice array, using a thin poly-methyl-methacrylate (PMMA) protection layer on top of the graphene film. The protection layer was removed after the wet chemical transfer following the recipe described in Ref. [71]. Therefore for our purposes the size of the single crystalline graphene domains should be appreciably larger than the orifice diameter, which ranges typically between 1 and 5 μm . The modified growth protocol reduces the graphene island nucleation rate and thus enlarges the G film domain size [75]. This is illustrated by the low energy electron microscopy (LEEM) image in Fig. 7b, where four rotational domains (colored red, green, blue and yellow) can be identified. The LEEM image clearly shows the existence of single domains larger than 10 μm , so that the achieved graphene quality appears appropriate for the construction of windows with width of a few microns that are covered by boundary free single crystalline graphene. To minimize graphene contamination, delamination and stress common for standard transfer protocols, we developed a process of controlled back-etching of the Cu supporting foil to avoid the use of any protection layer on top of the grown graphene film. Hence, clean suspended graphene membranes can be obtained that are in intimate contact with the remaining Cu support around the holes. In order to facilitate the process we used Cu foils structured on their backside in predefined areas by photolithography and partial Cu removal in a H_2SO_4 electrolyte which contained

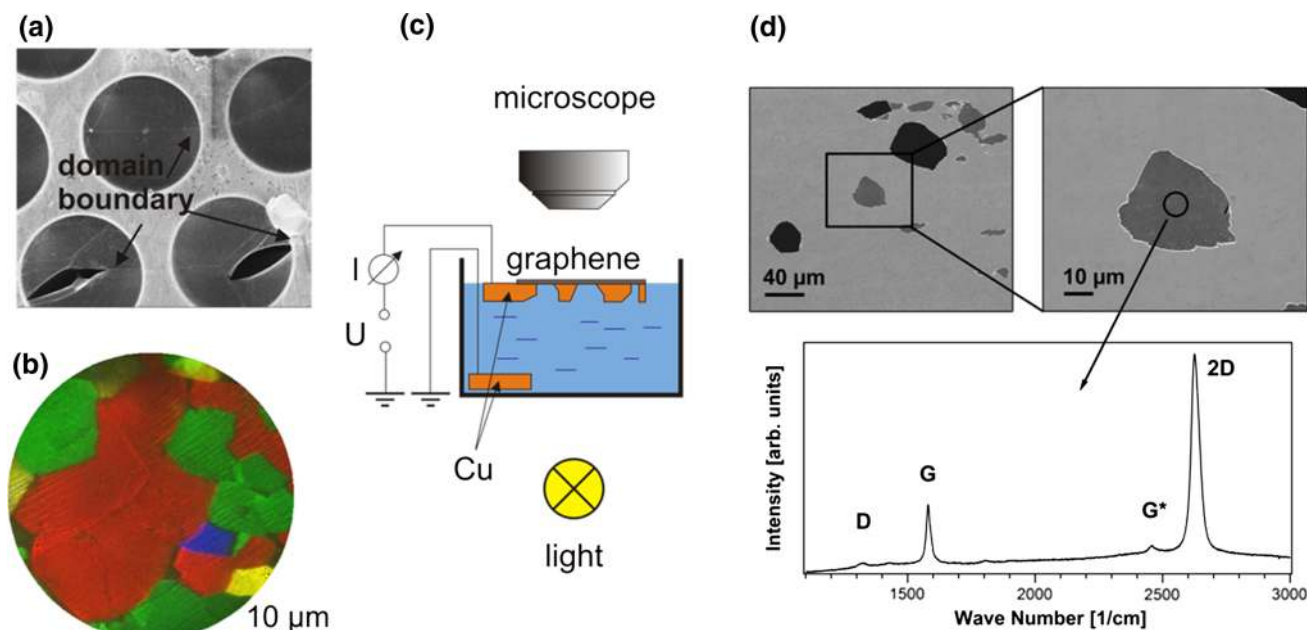


Fig. 7 **a** SEM (4 keV, In lens detector) image of a graphene monolayer (moderate quality) on an array of 4.5 μm orifices transferred using PMMA. After removing the PMMA protection layer, graphene exhibits a network of cracks along the domain boundaries. The typical domain size is of the order of a micrometer. **b** LEEM image of CVD grown graphene on Cu with an improved

0.1 M CuSO_4 . After removal of the photoresist and cleaning the Cu foil, the graphene was CVD grown on the front side of the Cu foil. The samples were then placed on the liquid electrolyte in a glass beaker, avoiding any contact of the graphene film with the solution, as sketched in Fig. 7c. By illuminating the beaker with light from the bottom, we terminated the electrochemical reaction when the etched holes appeared as bright spots in the transmission microscopy image. Since no protection layer was used, some of the suspended membranes collapsed during the electrolyte removal and drying, but many suspended membranes survived, as judged by the different grey level in the SEM images in Fig. 7d. The Raman spectra acquired locally on the suspended holes, showing the characteristic G-, G*- and 2D-bands and a very weak D-band, clearly identifies the membranes as a high quality G monolayer [76]. Raman spectroscopy and mapping of such samples is preferable to SEM imaging, where the electron beam can induce degradation of the graphene. While the completely gas tight E-cell still requires G membranes of 3–5 layers nominal thickness (see Sect. 4), efforts for improving the quality of monolayer thick G membranes for E-cells are ongoing [77,]. After optimizing the CVD growth of graphene on Cu [78–81], we are now capable of fabricating single crystalline graphene domains with diameters larger than 1 mm. Thus, one may even consider covering an array

of holes with monolayer graphene and sealing supports with multiple compartments or larger area holes that can be used beyond micro-focus applications. The electron transparency of such G membranes has already been tested with SPEM and is reported in the next Sect. 3.3.2.

3.3.2 Photoelectron Transparency of GO and G Membranes

In order to determine the transparency of GO and G membranes, we measured the photoelectron (PE) signal attenuation for membranes transferred to or grown on a supporting substrate. Ultrathin GO films were prepared via dip coating in a Langmuir–Blodgett assembly or drop casting of GO/water colloid solution onto an Au film deposited on a Si wafer (Au/Si wafer) [39]. As sketched in Fig. 8a, the obtained films contain patches of single or multilayer stacked GO platelets, separated by patches of the pristine Au surface.

A copper foil was used to obtain monolayer graphene, while G multilayers were grown by chemical vapor deposition (CVD) on a Ni/SiO₂/Si substrate. The multilayer graphene was chemically detached from the metal support and wet transferred onto the Au/Si wafer, using a standard PMMA-based protocol [71]. The transferred G layer covered only a part of the Au support, so there is an abrupt

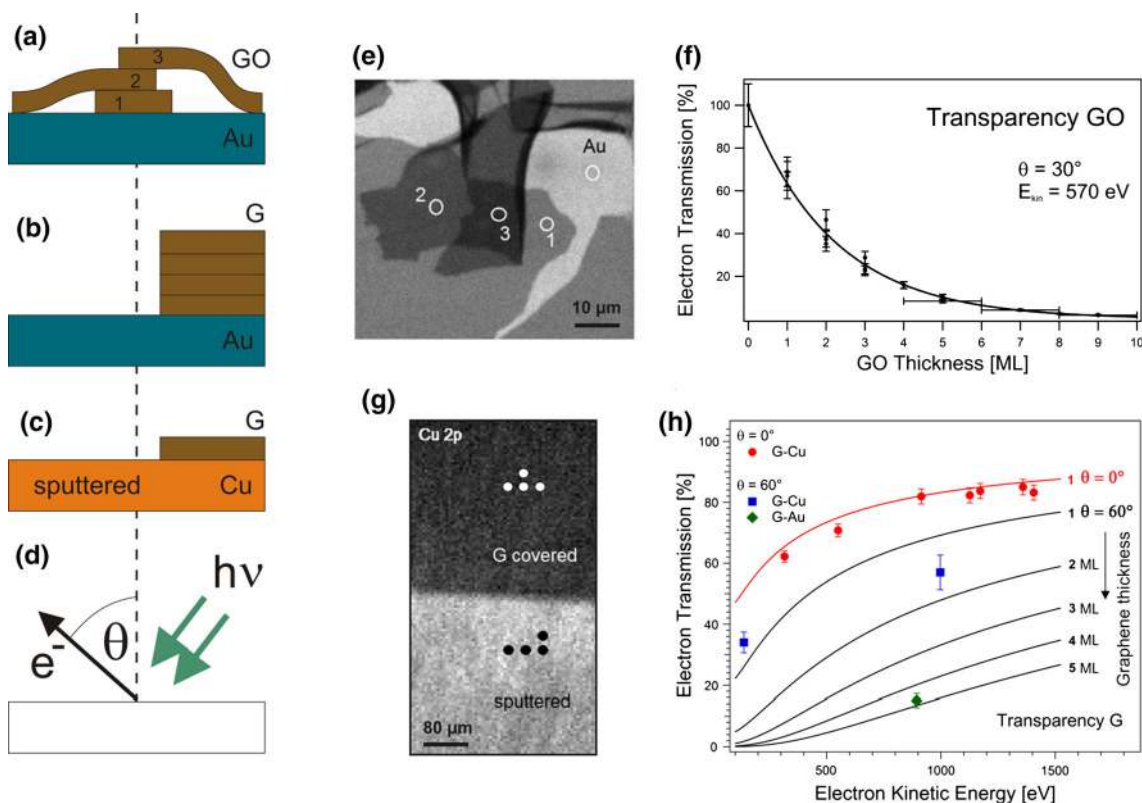


Fig. 8 a–c Different sample arrangements for electron attenuation measurements: **a** drop casted GO, **b** wet-transferred multilayer graphene on a Au film, **c** locally Ar⁺ etched monolayer graphene on Cu. **d** Geometry of the PE experiment; **e** Au 4f image (64 μm × 64 μm) of GO platelets on a Au film. Overlapped GO sheets (*dark*) consisting of 1, 2, 3 and more layers produce discrete contrast increase with respect to the pristine Au substrate (*light*); **f** Evaluated electron transparency of GO platelets for θ = 30° and E_{kin} = 570 eV. *Dots* represent independent measurements where the transmission could be determined with an error of about 10 %. GO

boundary between the G-covered and G-free Au (see Fig. 8b), which could be used for comparative PES analysis. Wet transfer protocols suffer from unavoidable contamination of the membrane material. To compare wet transferred membranes with the ultimately clean ones, we used the graphene layer grown on the Cu substrate, removing part of it via 1 keV Ar⁺ bombardment through a shadow-mask. This procedure resulted in a well-defined boundary between the contaminant-free G layer and a G-free Cu support surface (see Fig. 8c).

The local attenuation of the photoelectron signal, caused by the membrane material, was measured comparing the signal intensity from the G (GO)-covered and G (GO)-free parts of the supports. Using SPEM, it was possible to perform spectroscopic measurements in different location selected from the photoelectron images (see Fig. 8d). Figure 8e displays the Au image of the Au/Si surface covered by GO platelets of varying thicknesses generated

thickness larger than 5 layers is determined with an uncertainty of ±1 layer; **g**: Cu 2p image (320 μm × 640 μm) of the boundary between the graphene covered and sputter cleaned Cu foil. At the indicated spots local XPS spectra were acquired; **h**: Electron transparency of graphene at θ = 60° as a function of electron kinetic energy for different graphene thicknesses. The *top plot* corresponds to monolayer G-Cu and multilayer G-Au/Si. The *solid lines* (red: θ = 0° and black: θ = 60°) show the predicted attenuation curves calculated using the TPP-2 M formula [40, 82, 83]

by collecting the emitted Au 4f photoelectrons (PEs), while raster scanning the sample in front of the X-ray microprobe of 650 eV photon energy. The emitted PEs had a kinetic energy of ≈ 570 eV and were collected at an angle θ = 30° with respect to the surface normal. The grey-scale contrast level in Fig. 8e reflects the Au 4f signal attenuation by the GO platelets on top of the Au film and shows the discrete steps of electron transparency, correlated with the number of the stacked GO platelets. The plot in Fig. 8f clearly demonstrates the expected exponential decay of the electron transparency with the number n of the stacked platelets. This behavior is described by the well-known relationship:

$$\frac{I}{I_0} = \exp\left(-\frac{nd}{\lambda_{EAL}\cos(\theta)}\right) \quad (1)$$

where I/I₀ is the ratio between the signal intensity from GO-covered and GO-free surface, which is a measure of

the transparency, d is the layer thickness of a GO platelet, n is the number of GO layers and θ is the emission angle of the PEs (see Fig. 8d). λ_{EAL} is the effective attenuation length accounting for elastic scattering, routinely used instead of the inelastic mean free path λ_{IMFP} [82].

Our results have revealed that, for the given photon energy and geometry of photon illumination and electron emission at $\theta = 30^\circ$, the GO transparency for electrons with $E_{kin} = 570$ eV scales with the number of layers n as $(0.65)^n$. The same imaging approach was used in the case of the multilayer and monolayer graphene films on Au and Cu, respectively. Here, we illustrate only the results for the case of a Cu support, where the Cu 2p image was acquired using 1070 eV X-ray probe and an emission angle of $\theta = 60^\circ$ (see the micro-spots, indicated Fig. 8g, where both Cu 2p ($E_{kin} \approx 140$ eV) and Cu 3p ($E_{kin} \approx 1000$ eV) spectra were acquired as well). The corresponding electron transparencies versus the photoelectron kinetic energy obtained from this data set are shown as blue squares in the chart of Fig. 8h. The measured transparency of the multilayer G-Au film is also plotted (green diamond). In addition, transparency tests of monolayer G-Cu were performed using conventional Mg K_α and Al K_α radiation of laboratory X-ray sources and acquiring electron emission originated from the Cu 2p, Cu 3s and Cu 3p core levels and the Cu L_3VV Auger transition along the surface normal ($\theta = 0^\circ$). The results of these tests are also plotted in the chart of Fig. 8h (red circles) together with the expected signal attenuation curves for the two acquisition geometries (red: $\theta = 0^\circ$ and black: $\theta = 60^\circ$) for the indicated G-layer thickness as calculated using the so called TPP-2 M equation of Tanuma, Powell and Penn [40, 83, 84]. The theoretical curves are in fair agreement with the experimental points and indicate that for n -layer thick membranes electron transparencies better than $(0.5)^n$ are feasible by selecting a proper geometry and photoelectron kinetic energy.

We also tested the electron transparency of higher quality suspended G membranes, fabricated via CVD-grown graphene on Cu foil via local back etching of Cu substrate. Such membranes have a monolayer thickness, stronger adhesion to the substrate (compared to transferred graphene), minimal mechanical stress and do not contain the common PMMA-related contaminations. Figure 9a displays a representative SEM image of a locally back-etched G/Cu foil sample with one empty and three holes, covered with suspended graphene. The SPEM image of the same area, obtained by collecting Cu L_3VV Auger electrons, is displayed in the bottom panel of Fig. 9a, where the holes appear as darker areas as well.

The SPEM images can also contain important topographic information. As described in detail in our paper [42], for non-flat samples with topography that varies at the

micron scale, the local orientation of the sampled area with respect to the X-ray microprobe and the electron analyzer can lead to enhancement or attenuation (shadowing) of the photoelectron signal. In fact, the rather uniform brightness of the Cu L_3VV image (bottom panel in Fig. 9b) indicates that the Cu foil appears mostly flat, with an exception of the bright diagonal stripe (also present in SEM, see Fig. 9a). This stripe is a grain boundary of the Cu foil, which is inclined with respect to the rest of the Cu foil surface. As a result, also the membrane 3 grown over this area is inclined. As sketched in the lower panel in Fig. 9b, the inclination angle was found to be $\approx 60^\circ$ with respect to the X-ray microprobe (for details see the supporting information in Ref. [40]). It should be noted that the presence of differently inclined membranes on our samples is an asset that can be used for exploring the effect of geometry on the membrane transparency. The transparency of the membranes was evaluated by depositing thin Au films on their rear side and comparing the C 1s and Au 4f PES spectra of differently inclined membranes (2 and 3 in Fig. 9c). The lower panel in Fig. 9c shows the C 1s and Au 4f spectra, measured in locations 1, 2, 3 and normalized to the signal recorded from the membrane 2. Apparently, no Au 4f signal can be registered from the location 1 where Cu was not etched.

One can see that the C 1s intensities from supported (positions 1) and suspended graphene (position 2) are nearly the same, which indicates that both areas, oriented similarly to the X-ray microprobe, contain the same amount of carbon. This confirms that the wet back-etching of Cu substrate does not lead to a sensible enhancement of the carbonaceous contamination on the back of the membrane. In position 3, where the membrane is inclined by about 60° with respect to the X-ray microprobe, the C 1s signal is two times stronger, since in this geometry the irradiated area contributing to the C 1s signal is increased by a factor of $1/\cos(60^\circ)$. Comparing the C 1s spectra taken in locations 1, 2 and 3, one can notice that the peak positions are a bit different, which we attribute to some contribution of sp^3 -like carbon contaminants (introduced by electron irradiation during SEM imaging or during transportation of the samples through air), which lead to a C1s component at higher binding energy [85]. Since the contaminations reduce the electron transparency of the membranes, pristine or cleaned membranes should have transparencies better than those, derived in the present tests.

A good illustration of geometry effects on the electron transparency quantities is provided by comparing the Au 4f spectra from the Au deposited on the back of the membranes 2 and 3. The results in Fig. 9c clearly show that the Au 4f intensity for position 3 is higher more than three times. This is expected, since the inclination results in

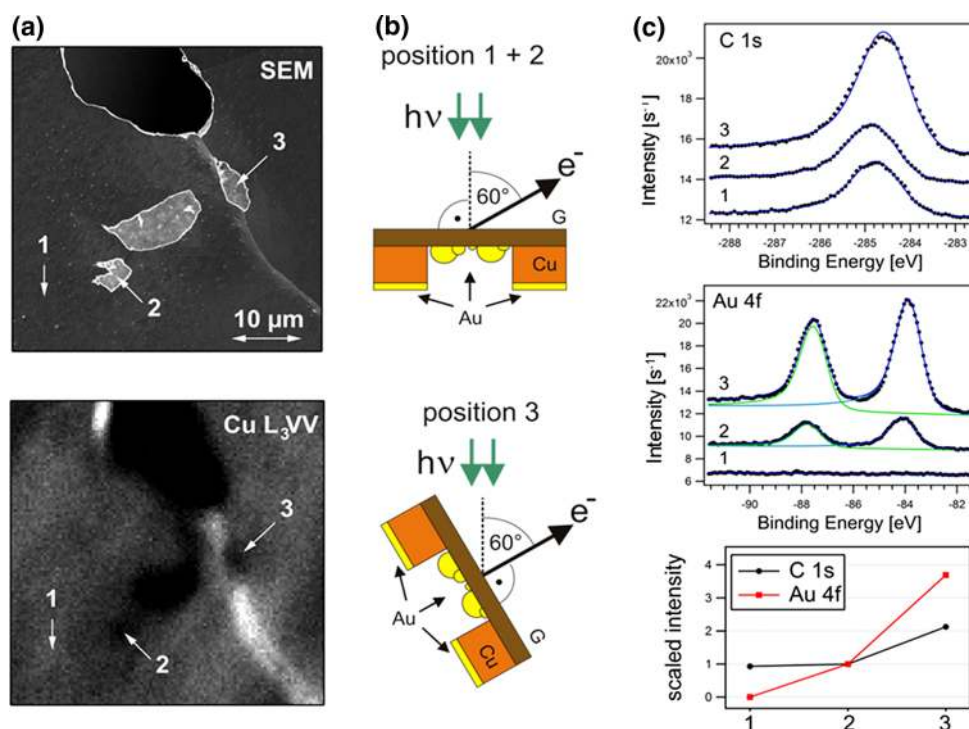


Fig. 9 **a** SEM, measured at 5 kV (*top*) and CuL₃VV SPEM image (*bottom*) of the G-Cu foil with empty and suspended holes. The *bright diagonal line* visible in both images indicates a grain boundary of the Cu foil, where the surface plane is inclined. The *numbers* indicate as grown graphene on the Cu substrate (1), suspended membrane (2) and suspended inclined membrane (3). **b** Sketch of the sample after Au evaporation on the membrane backside together with the local geometry with respect to the X-ray micro-probe and electron analyzer

photoelectron acceptance under normal emission, which increases the depth sensitivity, i.e. the contribution from bulk Au atoms to the Au 4f photoemission signal has increased.

Since the deposited Au on the membrane backside is not an uniformly thick layer, but rather consists of large hemispherical islands as on highly ordered pyrolytic graphite [86], we calculated the fraction x of the membrane backside, covered by Au islands. This was done by comparing the Cu 3p intensity from the Cu support at position 1 (not shown here) and the Au 4f intensity from location 2. This Cu 3p/Au 4f intensity ratio amounts to 0.67. Since both signals are similarly attenuated by the G monolayer their relative intensities can be related according to Eq. 2 under the assumption of a uniform film thickness and negligible elastic scattering (for details about XPS quantification [87]):

$$\frac{I_1(\text{Cu}3p)}{I_2(\text{Au}4f)} = 0.67 = \frac{1}{x} \times \frac{\rho(\text{Cu})}{\rho(\text{Au})} \times \frac{\sigma(\text{Cu}3p)}{\sigma(\text{Au}4f)} \times \frac{1 + \beta_{\text{Cu}3p}}{1 + \beta_{\text{Au}4f}} \times \frac{K_{\text{Cu}}}{K_{\text{Au}}} \quad (2)$$

corresponding to 1, 2 (*top*) and 3 (*bottom*). (c) C 1s (*top*) and Au 4f (*middle*) spectra acquired from locations 1, 2 and 3 after Au deposition on the sample backside and the corresponding peak intensities scaled to the ones measured in position 2 (*bottom*). Due to the different sample alignment and the grazing geometry of the SEM secondary electron detector, the Cu support appears slightly darker than the G-membranes compared to the SEM images presented in Fig. 7

Thus, we can determine the fraction x of the G membrane backside, covered by Au islands, using known values for the density ρ , the photo-ionization cross section σ , the corresponding asymmetry factor β for the angle between the photon beam and the electron emission angle (60° in this case), the layer thickness d , the inelastic mean free path λ , and $K = [1 - \exp(d/\lambda \cos 60^\circ)]^{-1}$ the bulk photoemission signal contribution for Au and for Cu at the given kinetic electron energy of the acquired photoelectrons. Considering the atom density of the (100) textured Cu foil [88] with a lattice constant of 3.61 Å and a layer distance $d = 1.81$ Å and the (111) nature of the Au islands [86] with a lattice constant of 4.08 Å and a layer thickness $d = 2.36$ Å, and all other values reported in Table 1, we estimated that about $x = 32\%$ of the membrane's back surface is covered with Au islands.

Using this number, we can estimate the detection limit of the Au 4f emission through the monolayer G membrane. Conservatively assuming that the detectable Au 4f signal should have an intensity that is 3 times the noise level measured in position 1, we obtain that Au islands covering a membrane fraction x of $\approx 0.4\%$ should be detectable. In

Table 1 Photoionization cross section, asymmetry factor of the core level ionization for the angle of 60° between X-ray beam and electron emission detection in the SPEM and the inelastic mean free path of the Cu 3p and Au 4f photoelectrons at the given kinetic energies

	E_{kin} (eV)	λ_{Cu} in Cu (Å)	λ_{Au} in Au (Å)	σ (10^{-18} cm 2)	β
Au 4f	894		12.9	0.8	0.959
Cu 3p	903	16.3		0.08	1.582

The data were taken from the literature [89, 90]

the case when the thickness of Au islands is comparable or smaller than the photoelectron IMFP, the PES sensitivity will be reduced by a factor of $K_{\text{Au}} = 3.3$ so the detection limit becomes $\approx 1\%$ Au. We want to point out that one can extend the measurement time (the acquisition time of the displayed Au 4f spectrum required less than 3 min) and increase the sensitivity so that using the single layer graphene membrane, an Au coverage well below 1% of a monolayer can be detected. Although many elements have photo-ionization cross sections significantly lower than the one of the Au 4f level, the presented data clearly show the potential of detecting sub-monolayer quantities by membrane based APPEES.

4 First AP-SPEM Experiments Through 2D Membranes

4.1 Membrane-Based Cells for SPEM Studies

We have tested two different cell designs sealed with GO or G-membranes, as sketched in Fig. 10. The single use design (Fig. 10a) is based on a Si/Si₃N₄ chip with a 50–100 nm thick Si₃N₄ window. Using focused ion bombardment (FIB), a micro-orifice was drilled in the center of

the Si₃N₄ window and the hole was covered with a single or few G or GO layers. The compartment below the Si₃N₄ membrane can be filled with a liquid and sealed with an UV curable glue on a supporting Si plate for encapsulating the liquid inside.

Figure 10b shows the design of the other type environmental cell with exchangeable graphene membranes, mounted on a few micron wide orifice, which was laser or FIB drilled in a metal disc or a Si/Si₃N₄ membrane. A droplet of liquid can be placed onto the disk covered with the graphene window. A pressure-relief elastomer membrane (Fig. 10b) seals and isolates the sample from the vacuum and also reduces the pressure shocks inside the cell during pumping. One can store ≈ 20 μl of a liquid sample, which lasts from tens of minutes to hours, depending on the leakage rate of the compartment.

4.2 In Situ Observation of Water Radiolysis and Bubble Formation Under High Intensity Soft X-Ray Irradiation

To demonstrate the capability of the ambient pressure SPEM through a graphene membrane, we studied X-ray induced water radiolysis [40], a process widely explored in radiation chemistry and recently in electron microscopy of liquid water [91–94] and frozen hydrated samples [95]. It is known that irradiation of liquid water with X-rays generates ionized and excited molecular and radical species. Some of the long living products of radiolysis, such as (H₂), hydrogen peroxide (H₂O₂) and hydroxyl radicals (OH) accumulate [91] and may form micro-bubbles that can be observed with PES if they are located close to the graphene membrane. Figure 11a and b show the O 1s chemical maps, measured through a G membrane sealed 5 μm orifice before and after prolonged irradiation with focused ca 1000 eV X-rays. Panel (b) illustrates the change

Fig. 10 Design of a closed graphene/GO E-cell for APXPS studies. **a** single orifice disposable cell; **b** re-fillable cell with exchangeable graphene/GO membranes. In addition to SPEM, these cells can also be used for SEM studies in liquid ambient. Adapted from Refs. [39, 62]

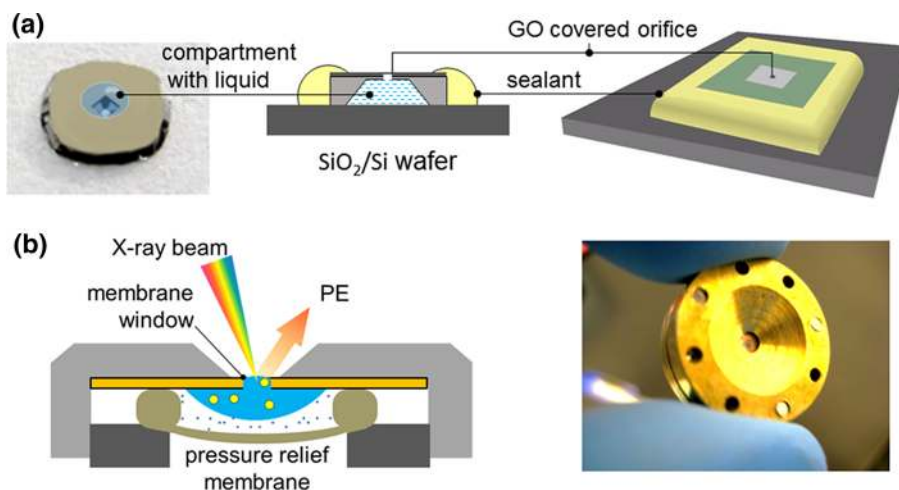
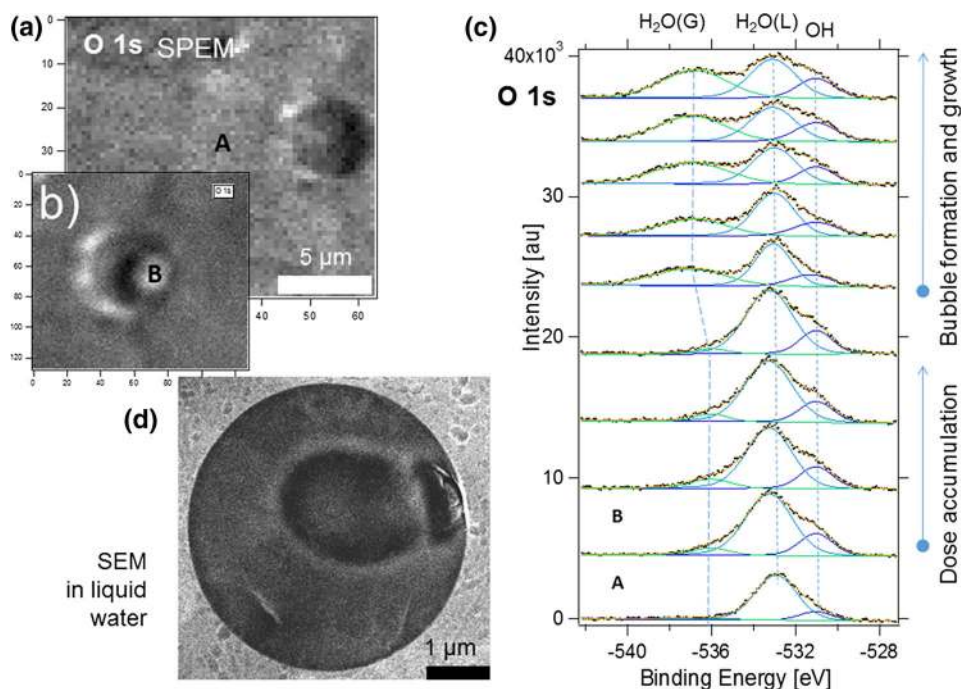


Fig. 11 **a** and **b** O 1s maps of water taken through a graphene-covered orifice before **(a)** and after **(b)** acquisition of spectra at the point B; The characteristic “shadow” on the left side of the feature B **(b)** indicates the change of the membrane topography; **c** bottom-up sequential O 1s spectra measured in location B showing the temporal evolution of the liquid (L) and vapor (G) components of water. For the sake of comparison the spectrum A recorded on the graphene covered support outside the membrane is displayed (point A in the left upper panel). **d** Liquid SEM images of the electron beam-induced gas bubble formation. Adapted from Ref. [40]



of topography at point B inside the membrane window, where the beam was positioned for the spectrum acquisition.

Figure 11c presents a set of sequentially measured O 1s spectra collected at the point B. For comparison, the bottom spectrum was taken in point A (Fig. 11a), which was a few tens of microns away from the membrane. The O 1s spectra were deconvoluted using three components, assigned to OH, H₂O (L) and H₂O (G), (here L and G stand for liquid and vapor, correspondingly) based on prior research [96, 97]. The presence of molecular water and hydroxyl adsorbed species beyond the orifice indicate that some water was trapped under the graphene during the wet transfer procedure or diffused from the orifice [40, 98, 99]. The evolution of the sequentially recorded O 1s spectra in Fig. 11c reveals that the O 1s G component appears and grows at the expense of the L one. This is an evidence of X-ray beam-induced micro-bubble formation underneath the membrane, which also is concomitant with topographical changes in the O 1s map in Fig. 11b. Similar electron beam induced bubble formation was also observed by SEM, as illustrated in Fig. 11d, where the lower electron yield from the bubble compared to liquid water accounts for the darker round area in the SEM image. We should note that upon prolonged irradiation the pressure of the bubble may increase until rupture of the membrane sets in. On the other hand, irradiation with soft X-rays does not affect the membrane stability itself. From a practical point of view, X-ray induced water radiolysis is an undesired

process, since it can obscure other interfacial processes and limits the lifetime of the membrane. Nevertheless, the results in Fig. 11 convincingly demonstrate the potential of APPES through graphene membranes to record spectral information from realistic liquid/solid interfaces with sub-micron lateral resolution. We should point out that the interest to exploring liquid/solid interfaces using APPES is growing very fast, preferentially using harder X-rays [100], and adding spatial resolution will be an asset.

4.3 In Situ Study of the Electrochemical Reaction

A current challenge in energy devices, such as batteries and fuel cells, is to understand the mechanisms of material degradation, which usually takes place and/or is initiated at the interfaces between working electrolytes and electrodes. Due to its high conductivity and intercalation ability sp² carbon based materials are often used in these devices. Among the carbonaceous materials, graphene, with its highest surface to volume ratio, is an ideal model electrode for accessing *in-operando* the processes occurring at carbonaceous electrodes/liquid electrolyte interfaces.

To test the feasibility of conducting PES electrochemical experiments with liquid electrolytes we designed an electrochemical cell with a graphene window that also acted as a working electrode. A droplet of AgNO₃ water solution was placed on the back side of the graphene window, and a silver counter electrode in contact with the droplet was also inserted (see Fig. 12a). The Ag 3d spectra were recorded

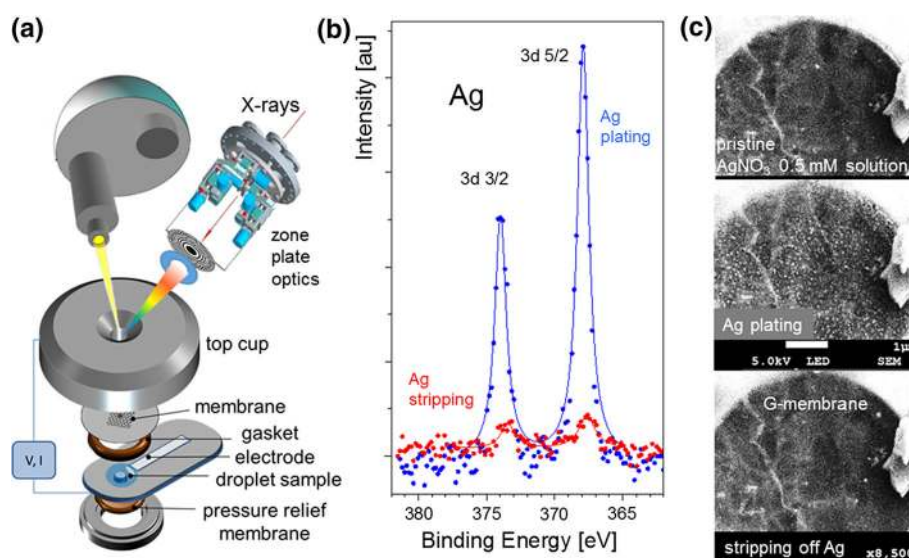


Fig. 12 **a** Design of an electrochemical cell with an electron transparent graphene window; **b** Ag 3d spectra recorded at the graphene membrane/AgNO₃ interface at two different potentials between working (graphene) and counter (Ag) electrodes. The *top* spectrum (*blue*) corresponds to the plating reaction while the *bottom*

one (*red*) corresponds to Ag stripping; **c** the concomitant liquid SEM studies of the same reaction in the same setup. The *top panel* is the initial state of the graphene electrode before applying a potential. The *middle and bottom panels* show the data for applied potentials of +3 V and −3 V, respectively, to the Ag counter-electrode

from the graphene-covered orifice after applying an appropriate positive or negative potential on the Ag counter-electrode so that the graphene working electrode can play the role of an anode or cathode. The spectra displayed in Fig. 12b demonstrate the expected growth of the Ag 3d peak intensity, when the graphene acts as an anode and Ag is electrodeposited according to the induced plating reaction. When the potential was reversed, the graphene membrane acts as a cathode so the Ag 3d intensity drops drastically due to the stripping of the Ag deposit. Figure 12c displays the SEM images of the processes confirming the SPEM results. The SEM image shows how small Ag clusters nucleate and grow on the graphene surface, when the positive potential is applied to the Ag counter electrode and how these Ag clusters dissolve upon the application of the negative potential. These results demonstrate the applicability of soft X-ray APPES for exploring in situ electrochemical processes in liquid electrolytes.

5 Outlook

The demands for APPES studies in liquids, solid/liquid, and at solid/gaseous interfaces at elevated gas pressures are growing fast, coming from the traditional research fields of catalysis, corrosion and electrochemistry as well as from emerging newer fields such as bio-medical research.

The superior versatility of synchrotron (SR) based APPES systems, where also the use of harder X-rays has

already been successfully demonstrated [101], have already made synchrotron-based APPES one of the most requested instruments at large facilities [17]. In fact, hard X-rays allow for experiments with enclosed or microfluidic cells which employ standard (10–20) nm thin Si₃N₄ membranes [30]. Undoubtedly, the limited beamtime available at the large-scale facilities requires parallel development of affordable laboratory based APPES instrumentation that can be used for less demanding conditions with the trade-offs in acquisition time and spectral resolution.

In this article, we reviewed the progress that has been made in APPES with submicron lateral resolution and converting SPEM into AP-SPEM by using several approaches. Indeed, the SPEM instruments can be operated only at synchrotron facilities, but they provide unique opportunities to explore materials and interfacial processes at their natural length scale. Adding the lateral resolution is the prerogative for understanding the important size–structure–function correlations, required for design and controlled fabrication of smart functional nanomaterials. Our overview of possible approaches for in-operando SPEM experiments, supported by experimental results, clearly suggests that the most promising and versatile approach is based on the use of electron transparent membranes. In this respect, the great advantage of using a sub-microprobe beam in SPEM is that it does not require fabrication of graphene or other electron transparent membranes larger than a few micrometers. Based on the obtained results with different samples and environments,

we envision at least three directions where activities and developments should be focused in the near future:

5.1 Radiation-Induced Effects in Liquids

The chemical and physical aspects of the interaction of high intensity X-ray beams with liquids are still poorly understood, but this information is needed when exploring the behavior of solid functional materials exposed to liquid ambient. Extensive investigations of X-ray radiation-induced processes at liquid/solid interfaces are required for exploring the surface chemistry in different liquids and their effects on the properties of the immersed objects. In particular, spatial and temporal distributions of the radiation-induced formation of reactive species can be crucial for interpreting interfacial processes in operating electrochemical and fuel cells, as well as in biological objects.

5.2 Liquid Cells Designs

Accumulated knowledge from soft X-ray microscopy based on X-ray transmission and X-ray photon-in/photon-out spectroscopy [102], and also recently from electron microscopy [103], using Si_3N_4 windows for a variety of sample set-ups is very helpful for application in hard X-ray APPEs, where the IMFP allows for developing environmental cells with Si_3N_4 windows of thickness of (10–20) nm. The cell's design should follow the current trends, i.e. several optimized designs adaptable to a specific set of experiments exploring, e.g. electrical, micromechanical, thermal, electrochemical and fluidic events. In the case of fluidic cells, since the needed amount of liquids for APPEs is rather small, the next generation of liquid cells could be disposable monolithic chips with on-board fluidics, where the liquid source together with electrophoretic, electroosmotic or micromechanical pumps are the integral parts of the lab-on-chip technology. Another trend in the e-cells designs could be the incorporation of additional options for in situ correlative spectroscopies and microscopies (luminescence, IR, Raman, etc.), using for example fiber optics.

5.3 Membranes made of 2D Materials

As discussed above, many of the novel 2D materials possess ultimately high electron transparency, high mechanical strength and can be fabricated at large yield. Therefore, these materials will continue to be an object of active research and technical developments as prospective windows for APPEs. However, since the purity control and delamination issues of transferred membranes can impede these applications, the future of 2D membrane windows depends on advances in wafer scale fabrication and

transfer-free protocols, where the support substrate can also be converted to a frame supporting the suspended membranes. The feasibility of fabrication of such single-layer graphene windows via local back etching of a Cu substrate has already been demonstrated, as reported above. The outstanding challenge for laboratory based (not microscopic) APPEs is the need for large area 2D membranes in measurements with an X-ray beam width of a few hundreds microns. The apparent solution that can be used for 2D materials is the fabrication of an array of multiple orifices covered with a 2D membrane. One possible design, depicted in Fig. 13, is a graphene based liquid cell.

The cell is based on a lithographically defined multi-channel or microporous matrix, which contains a high density of isolated or interconnected microfluidic channels. The channels, a few microns in size, are covered with a graphene membrane. The experimentally demonstrated effective graphene coverage in such a multi-hole sample can exceed 95 % (see Fig. 13). This allows for using standard PES instruments with a X-ray beam width up to 1 mm and preserving acceptable vacuum conditions even if parasitic effusion proceeds through a few open channels. Such multi-channel cells can be equipped with heaters and electrodes, as well as coupled with an on-board fluidic management system with sufficient amount of liquid to feed the micro-channels. We note that similar considerations and designs can be applied in an alternative membrane-based APPEs, where the membrane protects the entrance of the electron energy analyzer (see Fig. 1).

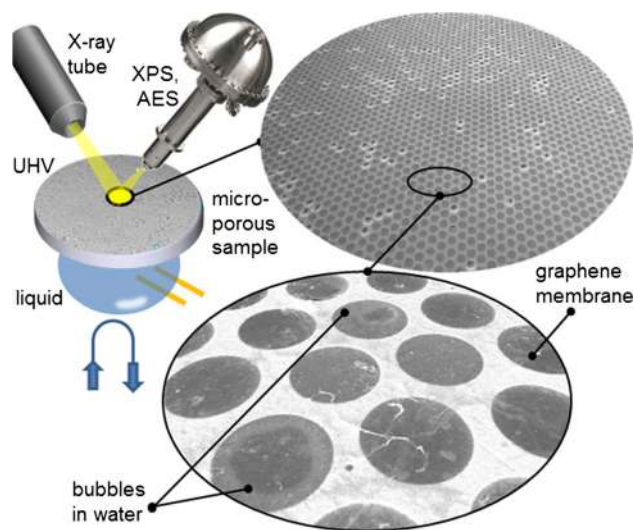


Fig. 13 Prospective design of a microchannel sample platform for laboratory APXPS, where a macroscopic array of liquid filled micro-channels or micro-pores is covered with a graphene membrane. SEM images of a graphene covered microchannel sample filled with liquid water. The diameter of each channel is 2 to 5 μm

Acknowledgments The authors acknowledge the invaluable contributions of A. Yulaev (NIST/UMD), J. Kraus (TUM), I. Vlasiouk (ORNL), M. Amati (Elettra), M. Abyaneh (now at Diamond SR source), B. Bozzini and I. Sgura (both at U. del Salento) who actively participated in developing and testing the reviewed set-ups. The financial support of SPEM experiments by ELETTRA is greatly acknowledged. S. Guenther acknowledges financial support within the framework of the priority program Graphene SPP 1459 of the German Science Foundation (DFG). The critical reading of the manuscript by C. Powell, N. Zhitenev and J. Unguris (all at NIST) are gratefully acknowledged.

Open Access This article is distributed under the terms of the Creative Commons Attribution 4.0 International License (<http://creativecommons.org/licenses/by/4.0/>), which permits unrestricted use, distribution, and reproduction in any medium, provided you give appropriate credit to the original author(s) and the source, provide a link to the Creative Commons license, and indicate if changes were made.

References

- Siegbahn K (1990) From X-ray to electron spectroscopy and new trends. *J Electron Spectrosc Relat Phenom* 51:11–36. doi:10.1016/0368-2048(90)80139-2
- Winter B, Faubel M (2006) Photoemission from liquid aqueous solutions. *Chem Rev* 106(4):1176–1211
- Siegbahn H, Asplund L, Kelfve P, Hamrin K, Karlsson L, Siegbahn K (1974) ESCA applied to liquids. II. Valence and core electron spectra of formamide. *J Electron Spectrosc Relat Phenom* 5(1):1059–1079
- Brown MA, Jordan I, Redondo AB, Kleibert A, Wörner HJ, van Bokhoven JA (2013) In situ photoelectron spectroscopy at the liquid/nanoparticle interface. *Surf Sci* 610:1–6
- Starr DE, Wong EK, Worsnop DR, Wilson KR, Bluhm H (2008) A combined droplet train and ambient pressure photoemission spectrometer for the investigation of liquid/vapor interfaces. *Phys Chem Chem Phys* 10(21):3093–3098
- Siegbahn H (1985) Electron spectroscopy for chemical analysis of liquids and solutions. *J Phys Chem* 89(6):897–909
- Jurgensen A, Esser N, Hergenroder R (2012) Near ambient pressure XPS with a conventional X-ray source. *Surf Interface Anal* 44(8):1100–1103. doi:10.1002/Sia.4826
- Tao F (2012) Operando studies of catalyst surfaces during catalysis and under reaction conditions: ambient pressure X-ray photoelectron spectroscopy with a flow-cell reactor. *Chemcatchem* 4(5):583–590. doi:10.1002/cctc.201200002
- Roy K, Vinod C, Gopinath CS (2013) Design and performance aspects of a custom-built ambient pressure photoelectron spectrometer toward bridging the pressure gap: oxidation of Cu, Ag, and Au surfaces at 1 mbar O₂ pressure. *J Phys Chem C* 117(9):4717–4726
- Pantförder J, Pöllmann S, Zhu J, Borgmann D, Denecke R, Steinrück H-P (2005) New setup for in situ X-ray photoelectron spectroscopy from ultrahigh vacuum to 1 mbar. *Rev Sci Instrum* 76(1):014102
- Eriksson SK, Hahlin M, Kahk JM, Villar-Garcia IJ, Webb MJ, Grennberg H, Yakimova R, Rensmo H, Edström K, Hagfeldt A, Siegbahn H, Edwards MOM, Karlsson PG, Backlund K, Åhlund J, Payne DJ (2014) A versatile photoelectron spectrometer for pressures up to 30 mbar. *Rev Sci Instrum* 85(7):075119. doi:10.1063/1.4890665
- Ogletree DF, Bluhm H, Lebedev G, Fadley CS, Hussain Z, Salmeron M (2002) A differentially pumped electrostatic lens system for photoemission studies in the millibar range. *Rev Sci Instrum* 73(11):3872–3877
- Bluhm H, Havecker M, Knop-Gericke A, Kiskinova M, Schlogl R, Salmeron M (2007) In situ X-ray photoelectron spectroscopy studies of gas/solid interfaces at near-ambient conditions. *Mater Res Soc Bull* 32(12):1022–1030. doi:10.1557/mrs.2007.211
- Schnadt J, Knudsen J, Andersen JN, Siegbahn H, Pietzsch A, Hennies F, Johansson N, Mårtensson N, Öhrwall G, Bahr S, Mähl S, Schaff O (2012) The new ambient-pressure X-ray photoelectron spectroscopy instrument at MAX-lab. *J Synchrotron Radiat* 19(5):701–704. doi:10.1107/s0909049512032700
- Grass ME, Karlsson PG, Aksoy F, Lundqvist M, Wannberg B, Mun BS, Hussain Z, Liu Z (2010) New ambient pressure photoemission end station at advanced light source beamline 9.3.2. *Rev Sci Instrum* 81(5):053106–053107
- Salmeron M, Schlögl R (2008) Ambient pressure photoelectron spectroscopy: a new tool for surface science and nanotechnology. *Surf Sci Rep* 63(4):169–199. doi:10.1016/j.surfrep.2008.01.001
- Starr D, Liu Z, Hävecker M, Knop-Gericke A, Bluhm H (2013) Investigation of solid/vapor interfaces using ambient pressure X-ray photoelectron spectroscopy. *Chem Soc Rev* 42:5833–5857
- Stöhr J (1992) NEXAFS spectroscopy. Springer, Berlin
- Powell CJ, Jablonski A (2009) Surface sensitivity of X-ray photoelectron spectroscopy. *Nucl Instrum Methods Phys Res Sect A* 601(1–2):54–65. doi:10.1016/j.nima.2008.12.103
- Stöhr J, Wu Y, Hermsmeier BD, Samant MG, Harp GR, Koranda S, Dunham D, Tonner BP (1993) Element-specific magnetic microscopy with circularly polarized X-rays. *Science* 259:658–661
- Stöhr J, Siegmann HC (2006) Magnetism: from fundamentals to nanoscale dynamics. Solid-state sciences. Springer, Berlin
- Kiskinova M (2000) Chemical characterization of surfaces and interfaces with submicron spatial resolution. *Surf Interface Anal* 30:464–471
- Günther S, Kaulich B, Gregoratti L, Kiskinova M (2002) Photoelectron microscopy and applications in surface and materials science. *Prog Surf Sci* 70(4–8):187–260. doi:10.1016/S0079-6816(02)00007-2
- Locatelli A, Bauer E (2008) Recent advances in chemical and magnetic imaging of surfaces and interfaces by XPEEM. *J Phys* 20:093002
- Barinov A, Dudin P, Gregoratti L, Locatelli A, Montes TO, Nino MA, Kiskinova M (2009) Synchrotron-based photoelectron microscopy. *Nucl Instrum Meth A* 601(1–2):195–202. doi:10.1016/j.nima.2008.12.157
- Kaya S, Ogasawara H, Näslund L-A, Forsell J-O, Sanchez Casalongue H, Miller DJ, Nilsson A (2013) Ambient-pressure photoelectron spectroscopy for heterogeneous catalysis and electrochemistry. *Catal Today* 205:101–105
- Ballarotto V, Breban M, Siegrist K, Phaneuf R, Williams E (2002) Photoelectron emission microscopy of ultrathin oxide covered devices. *J Vac Sci Technol B* 20(6):2514–2518
- Yang S-H, Mun B, Kay A, Kim S-K, Kortright J, Underwood J, Hussain Z, Fadley C (2000) Depth-resolved photoemission spectroscopy from surface and buried layers with soft X-ray standing waves. *Surf Sci* 461(1):L557–L564
- Wakita T, Taniuchi T, Ono K, Suzuki M, Kawamura N, Takagaki M, Miyagawa H, Guo F, Nakamura T, Muro T (2006) Hard X-ray photoelectron emission microscopy as tool for studying buried layers. *Jpn J Appl Phys* 45(3R):1886
- Kobayashi K (2009) Hard X-ray photoemission spectroscopy. *Nucl Instrum Methods Phys Res Sect A* 601(1):32–47

31. Briggs D, Seah MP (1983) Practical surface analysis by Auger and X-ray photoelectron spectroscopy. Wiley, New York
32. Jablonski A, Powell C (2009) Practical expressions for the mean escape depth, the information depth, and the effective attenuation length in Auger-electron spectroscopy and X-ray photoelectron spectroscopy. *J Vac Sci Technol A* 27(2):253–261
33. Jablonski A, Powell CJ (2015) Effective attenuation lengths for photoelectrons emitted by high-energy laboratory X-ray sources. *J Electron Spectrosc Relat Phenom* 199:27–37. doi:10.1016/j.elspec.2014.12.011
34. Smekal W, Werner WS, Powell CJ (2005) Simulation of electron spectra for surface analysis (SESSA): a novel software tool for quantitative Auger-electron spectroscopy and X-ray photoelectron spectroscopy. *Surf Interface Anal* 37(11):1059–1067
35. Masuda T, Yoshikawa H, Noguchi H, Kawasaki T, Kobata M, Kobayashi K, Uosaki K (2013) In situ X-ray photoelectron spectroscopy for electrochemical reactions in ordinary solvents. *Appl Phys Lett* 103(11):111604–111605
36. Tanuma S, Powell CJ, Penn DR (2011) Calculations of electron inelastic mean free paths. IX. Data for 41 elemental solids over the 50 eV to 30 keV range. *Surf Interface Anal* 43(3):689–713. doi:10.1002/sia.3522
37. Jennings SG (1988) The mean free path in air. *J Aerosol Sci* 19(2):159–166. doi:10.1016/0021-8502(88)90219-4
38. Kaulich B, Thibault P, Gianoncelli A, Kiskinova M (2011) Transmission and emission X-ray microscopy: operation modes, contrast mechanisms and applications. *J Phys* 23(8):083002
39. Kolmakov A, Dikin DA, Cote LJ, Huang J, Abyaneh MK, Amati M, Gregoratti L, Gunther S, Kiskinova M (2011) Graphene oxide windows for in situ environmental cell photoelectron spectroscopy. *Nat Nano* 6(10):651–657. doi:10.1038/nnano.2011.130
40. Kraus J, Reichelt R, Günther S, Gregoratti L, Amati M, Kiskinova M, Yulaev A, Vlassioug I, Kolmakov A (2014) Photoelectron spectroscopy of wet and gaseous samples through graphene membranes. *Nanoscale* 6(23):14394–14403. doi:10.1039/c4nr03561e
41. <http://www.elettra.trieste.it/it/lightsources/elettra/elettra-beamlines/esca-microscopy/esca-microscopy.html> (2015)
42. Günther S, Kolmakov A, Kovac J, Kiskinova M (1998) Artefact formation in scanning photoelectron emission microscopy. *Ultramicroscopy* 75(1):35–51
43. Dri C, Africh C, Esch F, Comelli G, Dubay O, Köller L, Kresse G, Dudin P, Kiskinova M (2006) Initial oxidation of the Rh(110) surface: ordered adsorption and surface oxide structures. *J Chem Phys* 125:9471
44. Gustafson J, Resta A, Mikkelsen A, Westerstrom R, Andersen JN, Lundgren E, Weissenrieder J, Schmidt M, Varga P, Kaspar N, Torrelles X, Ferrer S, Mittendorfer F, Kresse G (2006) Oxygen-induced step bunching and faceting of Rh(553): experiment and ab initio calculations. *Phys Rev B* 74:35401
45. Tolia AA, Smiley RJ, Delgass VN, Takoudis CG, Weaver MJ (1994) Surface oxidation of rhodium at ambient pressures as probed by surface-enhanced Raman and X-ray photoelectron spectroscopy. *J Catal* 150:56
46. Zhan RR, Vesselli E, Baraldi A, Lizzit S, Comelli G (2010) The Rh oxide ultrathin film on Rh(100): an X-ray photoelectron diffraction study. *J Chem Phys* 133:214701. doi:10.1063/1.3509777
47. Amati M, Kazemian Abyaneh M, Gregoratti L (2013) Dynamic high pressure: a novel approach toward near ambient pressure photoemission spectroscopy and spectromicroscopy. *J Instrum* 8(05):T05001
48. Blume R, Niehus H, Conrad H, Böttcher A, Aballe L, Gregoratti L, Barinov A, Kiskinova M (2005) Identification of subsurface oxygen species created during oxidation of Ru(0001). *J Phys Chem B* 109:14052
49. Bozzini B, Amati M, Gregoratti L, Mele C, Abyaneh MK, Prasciolu M, Kiskinova M (2012) In-situ photoelectron microscopy during the operation of a single-chamber SOFC. *Electrochem Commun* 24:104–107. doi:10.1016/j.elecom.2012.09.001
50. Bozzini B, Amati M, Gregoratti L, Kiskinova M (2013) In-situ photoelectron microspectroscopy and imaging of electrochemical processes at the electrodes of a self-driven cell. *Sci Rep* 3:2848. doi:10.1038/srep02848
51. Doh WH, Gregoratti L, Amati M, Zafeirotas S, Law YT, Neophytides SG, Orfanidi A, Kiskinova M, Savinova ER (2014) Scanning photoelectron microscopy study of the Pt/phosphoric-acid-imbibed membrane interface under polarization. *ChemElectroChem* 1:180–186
52. Drake IJ, Liu TC, Gilles M, Tyliczszak T, David Kilcoyne A, Shuh DK, Mathies RA, Bell AT (2004) An in situ cell for characterization of solids by soft X-ray absorption. *Rev Sci Instrum* 75(10):3242–3247
53. Guay D, Stewart-Ornstein J, Zhang X, Hitchcock AP (2005) In situ spatial and time-resolved studies of electrochemical reactions by scanning transmission X-ray microscopy. *Anal Chem* 77(11):3479–3487
54. Fuchs O, Zharnikov M, Weinhardt L, Blum M, Weigand M, Zubavichus Y, Bär M, Maier F, Denlinger J, Heske C (2008) Isotope and temperature effects in liquid water probed by X-ray absorption and resonant X-ray emission spectroscopy. *Phys Rev Lett* 100(2):027801
55. Tokushima T, Horikawa Y, Harada Y, Takahashi O, Hiraya A, Shin S (2009) Selective observation of the two oxygen atoms at different sites in the carboxyl group (–COOH) of liquid acetic acid. *Phys Chem Chem Phys* 11(11):1679–1682
56. Herranz T, Deng X, Cabot A, Guo J, Salmeron M (2009) Influence of the cobalt particle size in the CO hydrogenation reaction studied by in situ X-ray absorption spectroscopy. *J Phys Chem B* 113(31):10721–10727
57. Jiang P, Chen J-L, Borondics F, Glans P-A, West MW, Chang C-L, Salmeron M, Guo J (2010) In situ soft X-ray absorption spectroscopy investigation of electrochemical corrosion of copper in aqueous NaHCO₃ solution. *Electrochem Commun* 12(6):820–822
58. Masuda T, Yoshikawa H, Noguchi H, Kawasaki T, Kobata M, Kobayashi K, Uosaki K (2014) In situ X-ray photoelectron spectroscopy for electrochemical reactions at solid/liquid interfaces. In: Meeting Abstracts, 2014, vol 21. The Electrochemical Society, pp 887–887
59. Tsunemi E, Watanabe Y, Oji H, Cui Y-T, Son J-Y, Nakajima A (2015) Hard X-ray photoelectron spectroscopy using an environmental cell with silicon nitride membrane windows. *J Appl Phys* 117(23):234902. doi:10.1063/1.4922335
60. Takagi Y, Wang H, Uemura Y, Ikenaga E, Sekizawa O, Uruga T, Ohashi H, Senba Y, Yumoto H, Yamazaki H, Goto S, Tada M, Iwasawa Y, Yokoyama T (2014) In situ study of an oxidation reaction on a Pt/C electrode by ambient pressure hard X-ray photoelectron spectroscopy. *Appl Phys Lett* 105(13):131602. doi:10.1063/1.4897007
61. Park S, Ruoff RS (2009) Chemical methods for the production of graphenes. *Nat Nanotechnol* 4(4):217–224
62. Krueger M, Berg S, Stone DA, Strelcov E, Dikin DA, Kim J, Cote LJ, Huang J, Kolmakov A (2011) Drop-casted self-assembling graphene oxide membranes for scanning electron microscopy on wet and dense gaseous samples. *ACS Nano* 5(12):10047–10054. doi:10.1021/mn204287g
63. Nair R, Wu H, Jayaram P, Grigorieva I, Geim A (2012) Unimpeded permeation of water through helium-leak-tight graphene-based membranes. *Science* 335(6067):442–444

64. Li D, Müller MB, Gilje S, Kaner RB, Wallace GG (2008) Processable aqueous dispersions of graphene nanosheets. *Nat Nanotechnol* 3(2):101–105
65. Cote LJ, Kim J, Tung VC, Luo J, Kim F, Huang J (2010) Graphene oxide as surfactant sheets. *Pure Appl Chem* 83(1):95–110
66. Eda G, Fanchini G, Chhowalla M (2008) Large-area ultrathin films of reduced graphene oxide as a transparent and flexible electronic material. *Nat Nano* 3(5):270–274. doi:http://www.nature.com/nnano/journal/v3/n5/supinfo/nnano.2008.83_S1.html
67. Kim HW, Yoon HW, Yoon S-M, Yoo BM, Ahn BK, Cho YH, Shin HJ, Yang H, Paik U, Kwon S (2013) Selective gas transport through few-layered graphene and graphene oxide membranes. *Science* 342(6154):91–95
68. Joshi R, Carbone P, Wang F, Kravets V, Su Y, Grigorieva I, Wu H, Geim A, Nair R (2014) Precise and ultrafast molecular sieving through graphene oxide membranes. *Science* 343(6172):752–754
69. Bunch JS, Verbridge SS, Alden JS, van der Zande AM, Parpia JM, Craighead HG, McEuen PL (2008) Impermeable atomic membranes from graphene sheets. *Nano Lett* 8(8):2458–2462. doi:[10.1021/nl801457b](https://doi.org/10.1021/nl801457b)
70. Koenig SP, Boddeti NG, Dunn ML, Bunch JS (2011) Ultra-strong adhesion of graphene membranes. *Nat Nano* 6(9):543–546. doi:[10.1038/nnano.2011.123](https://doi.org/10.1038/nnano.2011.123)
71. Suk JW, Kitt A, Magnuson CW, Hao Y, Ahmed S, An J, Swan AK, Goldberg BB, Ruoff RS (2011) Transfer of CVD-grown monolayer graphene onto arbitrary substrates. *ACS Nano* 5(9):6916–6924. doi:[10.1021/nn201207c](https://doi.org/10.1021/nn201207c)
72. Castro Neto AH, Guinea F, Peres NMR, Novoselov KS, Geim AK (2009) The electronic properties of graphene. *Rev Mod Phys* 81(1):109–162
73. Huang PY, Ruiz-Vargas CS, van der Zande AM, Whitney WS, Levendorf MP, Kevek JW, Garg S, Alden JS, Hustedt CJ, Zhu Y, Park J, McEuen PL, Muller DA (2011) Grains and grain boundaries in single-layer graphene atomic patchwork quilts. *Nature* 469(7330):389–392. doi:[10.1038/nature09718](https://doi.org/10.1038/nature09718)
74. Li X, Cai W, An J, Kim S, Nah J, Yang D, Piner R, Velamakanni A, Jung I, Tutuc E, Banerjee SK, Colombo L, Ruoff RS (2009) Large-area synthesis of high-quality and uniform graphene films on copper foils. *Science* 324(5932):1312–1314
75. Kraus J, Böcklein S, Reichelt R, Günther S, Santos B, Menten TO, Locatelli A (2013) Towards the perfect graphene membrane? Improvement and limits during formation of high quality graphene grown on Cu-foils. *Carbon* 64:377–390. doi:[10.1016/j.carbon.2013.07.090](https://doi.org/10.1016/j.carbon.2013.07.090)
76. Malard LM, Pimenta MA, Dresselhaus G, Dresselhaus MS (2009) Raman spectroscopy in graphene. *Phys Rep* 473(5–6):51–87. doi:[10.1016/j.physrep.2009.02.003](https://doi.org/10.1016/j.physrep.2009.02.003)
77. Kraus J (2012) Optimierung des Graphenwachstums auf Kupfer zur Erzeugung graphenbasierter Membranen/Towards graphene based membranes: Optimizing graphene growth on copper. Technische Universität München, Garching, Master
78. Kraus J, Böbel M, Günther S (2016) Suppressing graphene nucleation during CVD on polycrystalline Cu by controlling the carbon content of the support foils. *Carbon* 96:153–165. doi:[10.1016/j.carbon.2015.09.048](https://doi.org/10.1016/j.carbon.2015.09.048)
79. Wang H, Wang G, Bao P, Yang S, Zhu W, Xie X, Zhang W-J (2012) Controllable synthesis of submillimeter single-crystal monolayer graphene domains on copper foils by suppressing nucleation. *J Am Chem Soc*. doi:[10.1021/ja2105976](https://doi.org/10.1021/ja2105976)
80. Yan Z, Lin J, Peng Z, Sun Z, Zhu Y, Li L, Xiang C, Samuel EL, Kittrell C, Tour JM (2012) Toward the synthesis of wafer-scale single-crystal graphene on copper foils. *ACS Nano* 6(10):9110–9117. doi:[10.1021/nn303352k](https://doi.org/10.1021/nn303352k)
81. Gan L, Luo Z (2013) Turning off hydrogen to realize seeded growth of subcentimeter single-crystal graphene grains on copper. *ACS Nano* 7(10):9480–9488. doi:[10.1021/nm404393b](https://doi.org/10.1021/nm404393b)
82. Cumpson PJ, Seah MP (1997) Elastic scattering corrections in AES and XPS. II. Estimating attenuation lengths and conditions required for their valid use in overlayer/substrate experiments. *Surf Interface Anal* 25(6):430–446. doi:[10.1002/\(SICI\)1096-9918\(199706\)25:6<430::AID-SIA254>3.0.CO;2-7](https://doi.org/10.1002/(SICI)1096-9918(199706)25:6<430::AID-SIA254>3.0.CO;2-7)
83. Tanuma S, Powell CJ, Penn DR (1993) Calculations of electron inelastic mean free paths (IMFPs) IV. Evaluation of calculated IMFPs and of the predictive IMFP formula TPP-2 for electron energies between 50 and 2000 eV. *Surf Interface Anal* 20:77–89
84. Xu M, Fujita D, Gao J, Hanagata N (2010) Auger electron spectroscopy: a rational method for determining thickness of graphene films. *ACS Nano* 4(5):2937–2945
85. Kidambi PR, Bayer BC, Blume R, Wang Z-J, Baetz C, Weatherup RS, Willinger M-G, Schloegl R, Hofmann S (2013) Observing graphene grow: catalyst-graphene interactions during scalable graphene growth on polycrystalline copper. *Nano Lett* 13(10):4769–4778. doi:[10.1021/nl4023572](https://doi.org/10.1021/nl4023572)
86. Hövel H, Barke I (2006) Morphology and electronic structure of gold clusters on graphite: scanning-tunneling techniques and photoemission. *Prog Surf Sci* 81(2–3):53–111. doi:[10.1016/j.progsurf.2006.01.002](https://doi.org/10.1016/j.progsurf.2006.01.002)
87. Powell CJ, Jablonski A (2010) Progress in quantitative surface analysis by X-ray photoelectron spectroscopy: current status and perspectives. *J Electron Spectrosc Relat Phenom* 178–179:331–346. doi:[10.1016/j.elspec.2009.05.004](https://doi.org/10.1016/j.elspec.2009.05.004)
88. Wofford JM, Nie S, McCarty KF, Bartelt NC, Dubon OD (2010) Graphene Islands on Cu foils: the interplay between shape, orientation, and defects. *Nano Lett* 10(12):4890–4896. doi:[10.1021/nl102788f](https://doi.org/10.1021/nl102788f)
89. Tanuma S, Powell CJ, Penn DR (1991) Calculations of electron inelastic mean free paths II. Data for 27 elements over the 50–2000 eV range. *Surf Interface Anal* 17:26
90. Yeh JJ, Lindau I (1985) Atomic subshell photoionization cross sections and asymmetry parameters: 1 ≤ Z ≤ 103. *At Data Nucl Data Tables* 32:1–155
91. Royall C, Thiel B, Donald A (2001) Radiation damage of water in environmental scanning electron microscopy. *J Microsc* 204(3):185–195
92. Thiberge S, Zik O, Moses E (2004) An apparatus for imaging liquids, cells, and other wet samples in the scanning electron microscopy. *Rev Sci Instrum* 75(7):2280–2289
93. Stoll JD, Kolmakov A (2012) Electron transparent graphene windows for environmental scanning electron microscopy in liquids and dense gases. *Nanotechnology* 23(50):505704
94. Grogan JM, Schneider NM, Ross FM, Bau HH (2013) Bubble and pattern formation in liquid induced by an electron beam. *Nano Lett*. doi:[10.1021/nl404169a](https://doi.org/10.1021/nl404169a)
95. Leapman RD, Sun S (1995) Cryo-electron energy loss spectroscopy: observations on vitrified hydrated specimens and radiation damage. *Ultramicroscopy* 59(1):71–79
96. Parsons D, Matricardi V, Moretz R, Turner J (1974) Electron microscopy and diffraction of wet unstained and unfixed biological objects. *Advances in biological and medical physics* 15:161
97. Parsons DF (1974) Structure of wet specimens in electron microscopy. *Science* 186:407–414
98. Stolyarova E, Stolyarov D, Bolotin K, Ryu S, Liu L, Rim K, Klima M, Hybertsen M, Pogorelsky I, Pavlishin I (2008) Observation of graphene bubbles and effective mass transport under graphene films. *Nano Lett* 9(1):332–337
99. Xu K, Cao P, Heath JR (2010) Graphene visualizes the first water adlayers on mica at ambient conditions. *Science* 329(5996):1188–1191

100. Lichterman MF, Hu S, Richter MH, Crumlin EJ, Axnanda S, Favaro M, Drisdell W, Hussain Z, Mayer T, Brunshwig BS, Lewis NS, Liu Z, Lewerenz H-J (2015) Direct observation of the energetics at a semiconductor/liquid junction by operando X-ray photoelectron spectroscopy. *Energy Environ Sci*. doi:[10.1039/C5EE01014D](https://doi.org/10.1039/C5EE01014D)
101. Fadley CS, Nemšák S (2014) Some future perspectives in soft- and hard- X-ray photoemission. *J Electron Spectrosc Relat Phenom* 195:409–422. doi:[10.1016/j.elspec.2014.06.004](https://doi.org/10.1016/j.elspec.2014.06.004)
102. Bluhm H, Andersson K, Araki T, Benzerara K, Brown GE, Dynes JJ, Ghosal S, Gilles MK, Hansen HC, Hemminger JC, Hitchcock AP, Ketteler G, Kilcoyne ALD, Kneedler E, Lawrence JR, Leppard GG, Majzlam J, Mun BS, Myneni SCB, Nilsson A, Ogasawara H, Ogletree DF, Pecher K, Salmeron M, Shuh DK, Tonner B, Tylliszczak T, Warwick T, Yoon TH (2006) Soft X-ray microscopy and spectroscopy at the molecular environmental science beamline at the advanced light source. *J Electron Spectrosc Relat Phenom* 150(2–3):86–104. doi:[10.1016/j.elspec.2005.07.005](https://doi.org/10.1016/j.elspec.2005.07.005)
103. de Jonge N, Ross FM (2011) Electron microscopy of specimens in liquid. *Nat Nano* 6(11):695–704